

# A Continuous Adjoint Framework for Shape and Topology Optimization and their Synergistic Use

Evangelos M. Papoutsis-Kiachagias \*

and James R.L Koch †

and Konstantinos T. Gkaragkounis ‡

and Kyriakos C. Giannakoglou§

*Laboratory of Thermal Turbomachines, Parallel CFD & Optimization Unit*

*National Technical University of Athens (NTUA)*

*9, Heroon Polytechniou, NTUA Zografou Campus, 15780, Athens, Greece*

In fluid mechanics, two of the most widely used optimization approaches are shape and topology optimization, which are generally treated as mutually-exclusive. This paper presents a general continuous adjoint formulation for both shape and topology optimization, focusing on (a) crucial aspects of computing accurate shape sensitivity derivatives such as the differentiation of the turbulence model PDEs and the proper treatment of grid sensitivities and (b) a synergistic, sequential application of topology and shape optimization, in which topology is used to define a preliminary solution from which shape optimization can be initiated. To achieve this, a transition process is used to accurately represent and parameterize the topological solution with NURBS surfaces. The flow cases presented in this work and the in-house code pertaining to the optimization and transition process are implemented within OpenFOAM. Results from purely aerodynamic as well as multi-disciplinary applications including Conjugate Heat Transfer (CHT) are presented.

## I. Introduction

Shape optimization was initially introduced as a shape control technique to reduce an objective function<sup>1</sup> and relies on altering the original boundary shape and, thus, its flow solution. In the past the continuous adjoint method has been widely used to drive shape optimization loops.<sup>1-5</sup> However, in the literature of continuous adjoint methods for shape optimization, a number of assumptions during the derivation of the field adjoint equations and sensitivity derivatives (SD) expressions is usually made. Two of the most significant pertain to the differentiation (or absence thereof: the so-called “frozen turbulence” assumption) of the turbulence model PDEs<sup>3,6-8</sup> and to the treatment (or lack) of grid sensitivities.<sup>3,9,10</sup> In this paper, a continuous adjoint method that differentiates the turbulence model PDEs and treats the grid sensitivities via the imposition of additional restrictions to the Lagrangian is presented and the impact of commonly made assumptions in the accuracy of the computed SD is showcased.

Topology optimization, first proposed in Ref. 11 for structural mechanics, has been expanded to the field of fluid mechanics through the introduction of a source term into the Stokes,<sup>12-14</sup> laminar,<sup>15</sup> turbulent<sup>8</sup> steady and unsteady,<sup>16</sup> flow equations. This source term acts as a design variable for each grid cell and its corresponding field is controlled to minimize an objective function. The interested reader can find an overview of relevant topology optimization methods, focusing mainly on structural but including also multi-disciplinary applications in.<sup>17,18</sup> Topology optimization is commonly employed in fluid mechanics to develop optimal internal-flow paths between prescribed inlets and outlets according to provided objective functions,

---

\*Postdoctoral researcher, e-mail:vaggelisp@gmail.com

†PhD student, e-mail:kochjamesr@gmail.com

‡PhD student, e-mail:kogkar@hotmail.com

§Professor, e-mail:kgianna@central.ntua.gr, web page:<http://velos0.ltt.mech.ntua.gr/research/>

but itself produces solutions which are not necessarily CAD-compatible. In contrast, shape optimization may only alter boundaries of known connectivity to search for an optimal solution, but uses far fewer design variables than topology (i.e., the boundary nodal or control point coordinates instead of internal field values) and is inherently CAD-compatible if the parameters of the CAD model are used as the design variables. In addition, and unlike topology optimization, shape imposes proper flow boundary conditions, thus leading to a more physically accurate solution. Thus, a compelling avenue of research is to be able to process a topology solution accurately such that it becomes parameterized and to then use it to initialize a shape optimization process which further refines the solution. This process was presented for 2D flows in Ref. 19 and is expanded to a 3D approach in this paper.

The objective function gradients driving the employed topology and shape optimization methods are computed with the continuous adjoint method. Since the mathematical development of the continuous adjoint method for both topology and shape optimization is, to a large extent, common, a general framework for continuous adjoint-based optimization is presented in section II. In section II.A, the mathematical development of the continuous adjoint method is presented for both fluid flow and CHT problems, following three different formulations regarding grid sensitivities. For the sake of simplicity, the differentiation of the turbulence model PDEs is not presented in this section. Instead, this takes place in section II.B, where the impact of the turbulent viscosity variation is investigated. In section II.C, the development of the continuous adjoint method for topology optimization problems, employing the level set method, is presented. Without loss in generality, the study focuses on incompressible single-discipline flows, with a vectorial source-term being superimposed to the momentum equations. The process of transition from topology to shape optimization is presented in section III for 3D internal flows. Finally, in section IV an exemplary test case is presented to showcase the transition process which allows topology and shape to be used in synergy, and 3D aerodynamic and multi-disciplinary optimization problems are tackled. All software used to produce the work presented in this paper was programmed in OpenFOAM 2.3.1.

## II. A General Continuous Adjoint Framework for Single-and Multi-Disciplinary Optimization

In this section, a continuous adjoint framework, generalized for both shape and topology optimization, is presented in a unified way for incompressible fluid flow and CHT problems. To do so, a switch variable  $\mathcal{E}$  is introduced to distinguish between the cases in which only incompressible fluid flow is considered ( $\mathcal{E} = 0$ ) and the CHT ones ( $\mathcal{E} = 1$ ). In the latter, additional PDEs describing the heat transfer over the fluid and solid regions are solved along with the flow equations.

### A. Formulation of the continuous adjoint method for shape optimization

Let  $\Omega$  be the overall domain, consisting of either the (incompressible) fluid domain  $\Omega_F$  in single-disciplinary flow problems or both  $\Omega_F$  and  $\Omega_S$  (the solid domain) in CHT problems. The derivation of the adjoint equations, their corresponding boundary conditions and the sensitivity derivative (SD) expression starts by defining the augmented objective function (presented here for laminar flows)

$$L = J + \int_{\Omega_F} u_i R_{v_i} d\Omega + \int_{\Omega_F} q R_p d\Omega + \mathcal{E} \sum_{D=F,S} \int_{\Omega_D} T_a^D R_T^D d\Omega + \lambda \sum_{D=F,\mathcal{E}S} \int_{\Omega_D} m_{a,i}^D R_{m,i}^D d\Omega \quad (1)$$

with the objective function being  $J = J^F + J^S$ , where F and S stand for fluid and solid respectively.  $J^F$  is assumed to be defined only along the boundary  $S_F$  of  $\Omega_F$ , written in a general way as

$$J^F = \int_{S_F} J_{S,i}^F n_i dS = \int_{S_{F,W}} J_{S,W,i}^F n_i dS + \int_{S_{F,O}} J_{S,O,i}^F n_i dS \quad (2)$$

where  $S_F = S_{F,W} \cup S_{F,O}$ ,  $S_{F,W}$  is the solid wall,  $S_{F,O}$  any other boundary of  $\Omega_F$  and  $n_i$  the surface outward unit normal vector. Also,  $J^S$  is assumed to be defined only in the interior of  $\Omega_S$ , and is thus expressed as

$$J^S = \int_{\Omega_S} J_{\Omega}^S d\Omega \quad (3)$$

In addition to  $J$ ,  $L$  includes the integrals of the residuals of the continuity ( $R_p$ ), momentum ( $R_{v_i}$ ), heat transfer over  $\Omega_F$  ( $R_T^F$ ), heat conduction over  $\Omega_S$  ( $R_T^S$ ) and mesh movement ( $R_{m,i}^D$ ,  $D = F, S$ ) equations

$$R_p = -\frac{\partial v_j}{\partial x_j} = 0 \quad (4a)$$

$$R_{v_i} = v_j \frac{\partial v_i}{\partial x_j} - \frac{\partial \tau_{ij}}{\partial x_j} + \frac{\partial p}{\partial x_i} + f_i(\vec{v}, \vec{b}) = 0 \quad (4b)$$

$$R_T^F = \rho_F v_j c_p \frac{\partial T^F}{\partial x_j} + \rho_F \frac{v_j}{2} \frac{\partial v_k^2}{\partial x_j} - \frac{\partial}{\partial x_j} \left( \rho_F c_p a_{eff} \frac{\partial T^F}{\partial x_j} \right) = 0 \quad (4c)$$

$$R_T^S = -\frac{\partial}{\partial x_j} \left( k^S \frac{\partial T^S}{\partial x_j} \right) = 0 \quad (4d)$$

$$R_{m,i}^D = \frac{\partial}{\partial x_j} \left( \frac{\partial m_i^D}{\partial x_j} \right) = 0, \quad D = F, S \quad (4e)$$

multiplied by the adjoint pressure  $q$ , adjoint velocities  $u_i$ , adjoint temperatures  $T_a^F$ ,  $T_a^S$  (over  $\Omega_F$ ,  $\Omega_S$  respectively) fields and adjoint grid displacement fields  $m_{a,i}^D$ ,  $D = F, S$  respectively. Equations 4c and 4d are solved only in CHT problems. In Eqs. 4a to 4c,  $p$ ,  $v_i$ ,  $\tau_{ij}$  stand for the static pressure divided by the constant density  $\rho_F$ , velocity and stress components ( $\tau_{ij} = \nu_{eff} \left( \frac{\partial v_i}{\partial x_j} + \frac{\partial v_j}{\partial x_i} \right)$ ,  $\nu_{eff} = \nu + \nu_t$ ,  $\nu, \nu_t$  stand for the bulk and turbulent viscosities) respectively, whereas  $f_i(\vec{v}, \vec{b})$  represents any external force applied to the fluid; such a term becomes active in topology optimization by setting the switch variable  $\mu = 0$  (see section II.C). Regarding Eqs. 4c and 4d, the thermal diffusivity is  $\alpha_{eff} = \alpha + \alpha_t$ , where  $\alpha = \nu/Pr$  and  $\alpha_t = \nu_t/Pr_t$  ( $Pr$ ,  $Pr_t$  are the laminar and turbulent Prandtl numbers),  $T^F$  and  $T^S$  are the fluid and solid temperatures, respectively,  $c_p$  the specific heat transfer coefficient under constant pressure and  $k^S$  the thermal conductivity of the solid. Repeated indices imply summation. The coupling of Eqs. 4c and 4d is performed along the Fluid-Solid Interfaces (FSI), seen from  $\Omega_F$  and  $\Omega_S$  as  $\bar{S}_F$  and  $\bar{S}_S$  respectively, through the following conditions

$$k^S \frac{\partial T^S}{\partial n} \Big|_{\bar{S}_S} = -k^F \frac{\partial T^F}{\partial n} \Big|_{\bar{S}_F} \quad (5)$$

$$T^S \Big|_{\bar{S}_S} = T^F \Big|_{\bar{S}_F} \quad (6)$$

where  $k^F = \rho_F c_p (a + a_t)$ . Throughout this paper,  $\nu$ ,  $\rho_F$ ,  $c_p$ ,  $k^S$ ,  $Pr$  and  $Pr_t$  are assumed to be constant. In addition, in Eq. 4e,  $m_i^D$  ( $i = 1, 2, 3$ ) stand for the Cartesian displacements of grid nodes of  $\Omega_F$ ,  $\Omega_S$  and  $\lambda$  is a switch variable being equal either to unity or zero, depending on how the continuous adjoint method for shape optimization problems is developed (see sections II.A.1, II.A.2, and II.A.3).

In shape optimization, where the design variables,  $b_n$ ,  $n \in [1, N]$ , affect the shape of  $S$  ( $S = S_F \cup \mathcal{E}S_S$ ), the continuous adjoint method has historically been formulated in two different ways, referred to as *FI* and *SI*. This is an abbreviation introduced by the group of authors of this paper in a previous publication;<sup>10</sup> in a different terminology *FI* stands for the first continuous adjoint formulation presented in Ref. 20, whereas *SI*, which was introduced later,<sup>3,7,21</sup> is known as the ‘‘reduced gradient’’ adjoint formulation. Both give the same field adjoint equations and boundary conditions, yet different expressions for the gradient of  $J$  with respect to (w.r.t.)  $b_n$ . Recently, a new formulation referred to as the Enhanced-SI (E-SI)<sup>10</sup> which combines the advantages of both was developed. The mathematical formulation of each will be presented in sections II.A.1, II.A.2, and II.A.3. If  $\vec{b}$  does not affect  $S$ , as is the case in topology optimization, there is no distinction between the three formulations. Through the differentiation of Eq. 1 w.r.t. the design variables  $b_n$  and the standard way of developing the adjoint problems, the field adjoint equations can be derived; these can be

written as follows:<sup>5, 7, 10, 22</sup>

$$R_q = -\frac{\partial u_j}{\partial x_j} = 0 \quad (7a)$$

$$R_{u_i} = u_j \frac{\partial v_j}{\partial x_i} - \frac{\partial(v_j u_i)}{\partial x_j} - \frac{\partial \tau_{ij}^a}{\partial x_j} + \frac{\partial q}{\partial x_i} + u_k \frac{\partial f_k(\vec{v}, \vec{b})}{\partial v_i} + \mathcal{E} \left( \rho_F c_p T_a^F \frac{\partial T^F}{\partial x_i} + \rho_F T_a^F v_k \frac{\partial v_k}{\partial x_i} - \rho_F v_i v_k \frac{\partial T_a^F}{\partial x_k} \right) = 0, \quad i=1, 2, (3) \quad (7b)$$

$$R_{T_a^F}^F = -v_j \frac{\partial T_a^F}{\partial x_j} - \frac{\partial}{\partial x_j} \left( \alpha_{eff} \frac{\partial T_a^F}{\partial x_j} \right) = 0 \quad (7c)$$

$$R_{T_a^S}^S = -\frac{\partial}{\partial x_j} \left( k^S \frac{\partial T_a^S}{\partial x_j} \right) + \frac{\partial J_\Omega^S}{\partial T^S} = 0 \quad (7d)$$

where  $\tau_{ij}^a = \nu_{eff} \left( \frac{\partial u_i}{\partial x_j} + \frac{\partial u_j}{\partial x_i} \right)$  is the adjoint stress tensor. Equations 7c and 7d are solved only in CHT problems. A general sensitivity expression, incorporating all terms appearing in the three different adjoint formulations (*FI*, *SI*, *E-SI*), is given by the following equation (for its derivation, see Refs. 5, 7, 10, 22)

$$\frac{\delta J}{\delta b_n} = \mu \left[ (1 - \gamma) W_{1,n}(\mathcal{E}) + \gamma W_{2,n}(\lambda, \mathcal{E}) + W_{3,n}(\gamma, \mathcal{E}) \right] + (1 - \mu) W_{4,n} \quad (8)$$

where

$$W_{1,n}(\mathcal{E}) = \int_{\Omega_F} \left\{ -u_i v_j \frac{\partial v_i}{\partial x_k} - u_j \frac{\partial p}{\partial x_k} - \tau_{ij}^a \frac{\partial v_i}{\partial x_k} + u_i \frac{\partial \tau_{ij}}{\partial x_k} + q \frac{\partial v_j}{\partial x_k} \right\} \frac{\partial}{\partial x_j} \left( \frac{\delta x_k}{\delta b_n} \right) d\Omega + \mathcal{E} \left\{ \int_{\Omega_F} \rho_F \left[ -c_p T_a^F v_j \frac{\partial T^F}{\partial x_k} - T_a^F v_j v_i \frac{\partial v_i}{\partial x_k} - \alpha_{eff} c_p \frac{\partial T_a^F}{\partial x_j} \frac{\partial T^F}{\partial x_k} + c_p T_a^F \frac{\partial}{\partial x_k} \left( \alpha_{eff} \frac{\partial T^F}{\partial x_j} \right) \right] \frac{\partial}{\partial x_j} \left( \frac{\delta x_k}{\delta b_n} \right) d\Omega + \int_{\Omega_S} \left[ -k^S \frac{\partial T_a^S}{\partial x_j} \frac{\partial T^S}{\partial x_k} + k^S T_a^S \frac{\partial^2 T^S}{\partial x_j \partial x_k} \right] \frac{\partial}{\partial x_j} \left( \frac{\delta x_k}{\delta b_n} \right) d\Omega \right\} \quad (9)$$

$$W_{2,n}(\lambda, \mathcal{E}) = \int_{S_{F,W}} \left[ -\left( \tau_{ij}^a n_j - q n_i + \frac{\partial J_{S_{W,l}}^F}{\partial v_i} n_l \right) \frac{\partial v_i}{\partial x_k} + \frac{\partial J_{S_{W,i}}^F}{\partial x_k} n_i \right] \frac{\delta x_k}{\delta b_n} dS - \lambda \sum_{D=F, \mathcal{E}S} \left( \int_{S_{D,W}} \frac{\partial m_{a,k}^D}{\partial x_j} n_j \frac{\delta x_k}{\delta b_n} dS \right) + \mathcal{E} \left\{ -\int_{S_{S,D}} k^S \frac{\partial T_a^S}{\partial n} \frac{\partial T^S}{\partial x_k} \frac{\delta x_k}{\delta b_n} dS + \int_{S_{F,W^*}} k^F T_a^F \frac{\partial^2 T^F}{\partial x_j \partial x_k} n_j \frac{\delta x_k}{\delta b_n} dS + \int_{\bar{S}_F} \left[ T_a^F \left( k^F \frac{\partial^2 T^F}{\partial x_j \partial x_k} - k^S \frac{\partial^2 T^S}{\partial x_j \partial x_k} \right) n_j - k^F \frac{\partial T_a^F}{\partial x_j} n_j \left( \frac{\partial T^F}{\partial x_k} - \frac{\partial T^S}{\partial x_k} \right) \right] \frac{\delta x_k}{\delta b_n} dS \right\} \quad (10)$$

$$W_{3,n}(\gamma, \mathcal{E}) = \int_{S_{F,W}} J_{S_{W,i}}^F \frac{\delta(n_i dS)}{\delta b_n} - \int_{S_{F,W}} \left( -u_k n_k + \frac{\partial J_{S_{W,k}}^F}{\partial \tau_{lz}} n_k n_l n_z \right) \left( \tau_{ij} \frac{\delta(n_i n_j)}{\delta b_n} + \gamma \frac{\partial \tau_{ij}}{\partial x_k} \frac{\delta x_k}{\delta b_n} n_i n_j \right) dS - \int_{S_{F,W}} \frac{\partial J_{S_{W,k}}^F}{\partial \tau_{lz}} n_k t_l^I t_z^I \left( \tau_{ij} \frac{\delta(t_i^I t_j^I)}{\delta b_n} + \gamma \frac{\partial \tau_{ij}}{\partial x_k} \frac{\delta x_k}{\delta b_n} t_i^I t_j^I \right) dS - \int_{S_{F,W}} \left( \frac{\partial J_{S_{W,k}}^F}{\partial \tau_{lz}} n_k (t_l^I t_z^I + t_l^I t_z^I) \right) \left( \tau_{ij} \frac{\delta(t_i^I t_j^I)}{\delta b_n} + \gamma \frac{\partial \tau_{ij}}{\partial x_k} \frac{\delta x_k}{\delta b_n} t_i^I t_j^I \right) dS - \int_{S_{F,W}} \frac{\partial J_{S_{W,k}}^F}{\partial \tau_{lz}} n_k t_l^I t_z^I \left( \tau_{ij} \frac{\delta(t_i^I t_j^I)}{\delta b_n} + \gamma \frac{\partial \tau_{ij}}{\partial x_k} \frac{\delta x_k}{\delta b_n} t_i^I t_j^I \right) dS + \mathcal{E} \left\{ \int_{S_{F,W^*}} k^F T_a^F \frac{\partial T^F}{\partial x_j} \frac{\delta n_j}{\delta b_n} dS + \int_{\bar{S}_F} T_a^F \left( k^F \frac{\partial T^F}{\partial x_j} - k^S \frac{\partial T^S}{\partial x_j} \right) \frac{\delta n_j}{\delta b_n} dS + \int_{S_{S,Fl}} k^S T_a^S \frac{\partial T^S}{\partial x_j} \frac{\delta n_j}{\delta b_n} dS \right\} \quad (11)$$

$$W_{4,n} = \int_{\Omega_F} u_i \frac{\partial f_i}{\partial b_n} \Big|_{\vec{v}=ct} d\Omega \quad (12)$$

In the above equations,  $J_{S_{W,k}}^F$  is the part of the objective defined on the wall boundary of  $\Omega_F$  (see Eq. 2) and  $\mathbf{n}_j$  and  $\mathbf{t}^I$ ,  $\mathbf{l}=\mathbf{I}, \mathbf{II}$  the normal and tangent to the surface unit vectors, respectively. Also,  $S_{F,W^*}$

corresponds to the non-FSI walls of  $\Omega_F$  and  $S_{S,Fl}, S_{S,D}$  to boundaries of  $\Omega_S$  where constant heat-flux and fixed temperature is imposed, respectively. The remainder of this section focuses on the way each of the three sensitivity formulations is obtained.

### 1. The Field Integral (FI) Adjoint Formulation

The first formulation of the continuous adjoint method is known as the ‘‘Field Integral’’ adjoint formulation (*FI*) as it leads to gradient expressions with field integrals including variations in the spatial coordinates  $\vec{x}$  w.r.t.  $\vec{b}$ , a.k.a. grid sensitivities. To set-up the *FI* formulation, one should start from the total derivative of  $L$  Eq. 1, which for  $\lambda=0$  reads

$$\begin{aligned} \frac{\delta L}{\delta b_n} = & \frac{\delta J}{\delta b_n} + \int_{\Omega_F} \left( u_i \frac{\delta R_{v,i}}{\delta b_n} + q \frac{\delta R_p}{\delta b_n} + \mathcal{E} T_a^F \frac{\delta R_T^F}{\delta b_n} \right) d\Omega + \mathcal{E} \int_{\Omega_S} T_a^S \frac{\delta R_T^S}{\delta b_n} d\Omega \\ & + \int_{\Omega_F} (u_i R_{v,i} + q R_p + \mathcal{E} T_a^F R_T^F) \frac{\delta(d\Omega)}{\delta b_n} + \mathcal{E} \int_{\Omega_S} T_a^S R_T^S \frac{\delta(d\Omega)}{\delta b_n} \end{aligned} \quad (13)$$

where the last two integrals vanish since  $R_{v,i} = R_p = R_T^F = R_T^S = 0$  in  $\Omega_F$  and  $\Omega_S$ . By applying the chain rule, the formula  $\frac{\delta}{\delta b_n} \left( \frac{\partial \Phi}{\partial x_j} \right) = \frac{\partial}{\partial x_j} \left( \frac{\delta \Phi}{\delta b_n} \right) - \frac{\partial \Phi}{\partial x_k} \frac{\partial}{\partial x_j} \left( \frac{\delta x_k}{\delta b_n} \right)$  and the Green-Gauss theorem, the total derivatives (symbol  $\delta$ ) of  $R_{v,i}$ ,  $R_p$ ,  $R_T^F$ ,  $R_T^S$  w.r.t.  $b_n$  are expanded, leading to a formula involving integrals of expressions multiplied by  $\delta v_i/\delta b_n$ ,  $\delta p/\delta b_n$ ,  $\delta T^F/\delta b_n$ , and  $\delta T^S/\delta b_n$ . By zeroing those expressions in the volume integrals of  $\delta L/\delta b_n$  the field adjoint equations, Eqs. 7, for  $\Omega_F$  and  $\Omega_S$  are derived.<sup>10</sup> The adjoint boundary conditions arise by zeroing the expressions multiplying  $\delta p/\delta b_n$ ,  $\delta v_i/\delta b_n$ ,  $\delta \tau_{ij}/\delta b_n$ ,  $\delta T^F/\delta b_n$ , and  $\delta T^S/\delta b_n$  in the surface integrals of  $\delta L/\delta b_n$ , where necessary.<sup>23</sup> The remaining terms in  $\delta L/\delta b_n$  yield the SD expression, which is obtained through Eq. 8 by setting  $\gamma = \lambda = 0$  and  $\mu = 1$ . It should be noted that term  $W_{1,n}$ , given by Eq. 9 and included in Eq. 8, requires the computation of  $\delta x_k/\delta b_n$  for the entire flow domain, in single-disciplinary or in all domains in CHT problems. Two standard methods of computing the required grid sensitivities are finite differences (FD) or direct differentiation (DD) of the grid displacement model, both of which have a cost that scales linearly with the design variables number. Consequently, the *FI* adjoint method becomes computationally expensive in problems with many design variables.

### 2. The Surface Integral (SI) Adjoint Formulation

The ‘‘Surface Integral’’ (*SI*) formulation of the continuous adjoint method (often referred to as the ‘‘reduced-gradient’’ method<sup>21</sup>) was developed later on as a more viable alternative. In contrast to the *FI* formulation, this is based on the application of the Leibniz theorem (for domains the shape of which changes due to variations in  $b_n$ ), in order to develop the total derivative of Eq. 1 (for  $\lambda = 0$ ), leading to

$$\begin{aligned} \frac{\delta L}{\delta b_n} = & \frac{\delta J}{\delta b_n} + \int_{\Omega_F} \left( u_i \frac{\partial R_{v,i}}{\partial b_n} + q \frac{\partial R_p}{\partial b_n} + \mathcal{E} T_a^F \frac{\partial R_T^F}{\partial b_n} \right) d\Omega + \mathcal{E} \int_{\Omega_S} T_a^S \frac{\partial R_T^S}{\partial b_n} d\Omega \\ & + \int_{S_F} \left( u_i R_{v,i} + q R_p + \mathcal{E} T_a^F R_T^F \right) n_k \frac{\delta x_k}{\delta b_n} dS + \mathcal{E} \int_{S_S} T_a^S R_T^S n_k \frac{\delta x_k}{\delta b_n} dS \end{aligned} \quad (14)$$

where  $\partial/\partial b_n$  stands for the partial derivatives w.r.t. the design variables  $b_n$ . The last two integrals in Eq. 14 are usually ignored<sup>7</sup> by making the (unreliable; see below) assumption that the flow PDEs are satisfied along the boundary, yielding a severed form of Eq. 14. The *SI* formulation leads to the same field adjoint equations and boundary conditions as the *FI* one, but to a different SD expression; the latter containing only surface integrals after setting the switch variables of Eq. 8 as  $\gamma = \mu = 1$ ,  $\lambda = 0$ . Thus, the aptly-named *SI* formulation avoids the computation of grid sensitivities for the entire flow domain, being computationally cheaper than *FI* for this reason.

### 3. The Enhanced-SI (E-SI) Adjoint Formulation

The main difference between the *FI* and *SI* formulations is that the  $W_{1,n}$  term in Eq. 8 (the term containing the spatial gradient of the grid sensitivities) is retained when using the *FI* formulation, which can be costly to compute for a large  $N$ . On the other hand, *SI* though far less expensive than *FI* for problems with many design variables, cannot guarantee accurate (or even correctly signed) SD due to the elimination of

last two integrals in Eq. 14. The ‘‘Enhanced-*SI*’’ (E-*SI*) adjoint formulation, as firstly proposed in Ref. 10, intends to alleviate the accuracy issue of the *SI* formulation, while having almost the same low computational cost. In other words, the E-*SI* combines the main advantages of the *FI* and *SI* formulations by avoiding the computation of  $\delta x_k/\delta b_n$  at the internal nodes. This is achieved by extending the adjoint formulation through considering grid displacement PDEs as extra governing equations ( $\lambda = 1$  in Eq. 1); without loss in generality, a Laplace-based grid displacement model is assumed (see Eq. 4e). In order to eliminate the field integrals which include  $\delta x_k/\delta b_n$  in  $\delta L/\delta b_n$ , the adjoint grid displacement PDEs arise

$$R_{m_a,k}^F = \frac{\partial^2 m_{a,k}^F}{\partial x_j^2} - \frac{\partial}{\partial x_j} \left\{ u_i v_j \frac{\partial v_i}{\partial x_k} + \tau_{ij}^a \frac{\partial v_i}{\partial x_k} - u_i \frac{\partial \tau_{ij}}{\partial x_k} + u_j \frac{\partial p}{\partial x_k} + q \frac{\partial v_j}{\partial x_k} + \mathcal{E} \rho_F \left[ -c_p T_a^F v_j \frac{\partial T^F}{\partial x_k} - T_a^F v_j v_i \frac{\partial v_i}{\partial x_k} - \alpha_{eff} c_p \frac{\partial T_a^F}{\partial x_j} \frac{\partial T^F}{\partial x_k} + c_p T_a^F \frac{\partial}{\partial x_k} \left( \alpha_{eff} \frac{\partial T^F}{\partial x_j} \right) \right] \right\} = 0 \quad (15a)$$

$$R_{m_a,k}^S = \frac{\partial^2 m_{a,k}^S}{\partial x_j^2} - \frac{\partial}{\partial x_j} \left( k^S T_a^S \frac{\partial^2 T^S}{\partial x_j \partial x_k} - k^S \frac{\partial T_a^S}{\partial x_j} \frac{\partial T^S}{\partial x_k} \right) + J_{M,k}^S = 0 \quad (15b)$$

and should be satisfied in addition to the adjoint mean-flow (and turbulence model: see section II.B) PDEs. In Eq. 15b,  $J_{M,k}^S$  stands for the contributions of the differentiated  $J^S$  to the adjoint grid displacement equations of  $\Omega_S$ . After the appropriate mathematical development, the E-*SI* based SD is given by Eq. 8, by setting  $\mu = \gamma = \lambda = 1$ , including solely boundary integrals. The extra cost of computing SD using the E-*SI* instead of the *SI* formulation stems from the numerical solution of the adjoint grid displacement equations, Eqs. 15a and 15b, being negligible compared to that of solving the primal and adjoint PDEs. In addition, the two major advantages of the *SI* formulation remain valid for E-*SI*, as it has: (a) cost-independence from the number of design variables and (b) gradient computations based on surface integrals only. In table 1, the switch variables used in Eq. 8 are summarized.

	Shape	Topology
$\mu$	1	0

	Fluid	CHT
$\mathcal{E}$	0	1

	SI	E-SI	FI
$\gamma$	1	1	0
$\lambda$	0	1	0

**Table 1.** Values of switch variables  $\mathcal{E}$ ,  $\mu$ ,  $\lambda$ ,  $\gamma$ .

In figures 1 and 2, the SD computed with the three different adjoint formulations are compared in an internal and an external aerodynamics shape optimization problem, summarizing the merits of using the E-*SI* formulation. Even if the above theory has been presented for laminar flows, both single-disciplinary presented cases concern turbulent flows by also considering material that can be found in section II.B. In figure 3, SD are computed for a CHT problem. This problem involves the laminar flow in an S-bend duct attached to a solid body. It can be noticed that the *SI* adjoint provide, even for such a simple test case, quite inaccurate sensitivities.

## B. Continuous Adjoint to Turbulence Model PDEs

In the literature of continuous adjoint methods for turbulent flows, a standard practice in the majority of published works is to assume ‘‘frozen turbulence’’, i.e. to neglect variations in the turbulent viscosity as if changes in the shape of the aerodynamic body affect only the mean flow quantities. This assumption occasionally results in SD which are wrongly signed and, thereby, seriously affect the optimization process. It is obvious, then, that a rigorous approach should include the differentiation of the turbulence model equation(s) w.r.t. the design variables. This requires the formulation and solution of the adjoint to the turbulence model PDEs, the continuous forms of which have been developed for three turbulence models; Spalart–Allmaras,<sup>24</sup> k- $\epsilon$ ,<sup>25</sup> and k- $\omega$  SST<sup>26</sup> (see also Ref. 5).

If, for instance, it was assumed that closure is effected by the one-equation Spalart–Allmaras model, the development of the adjoint *SI* formulation would begin by adding  $\int_{\Omega_F} \tilde{\nu}_a R_{\bar{\nu}} d\Omega$  to the RHS of Eq. 1,

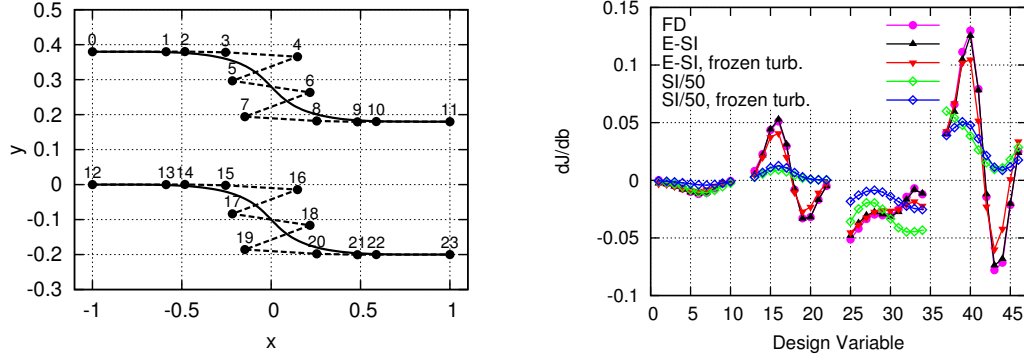


Figure 1. Turbulent flow case in an S-bend duct ( $Re=10^5$ ), using the  $k-\omega$  SST model and targeting minimum total pressure losses. (a) Duct geometry (not in scale) and parameterization using 24 Bézier–Bernstein control points. (b) Total pressure losses SD w.r.t. the Bézier–Bernstein control point coordinates, computed using the E-SI and SI formulations, in comparison with finite differences (FD), considered to give the “reference” SD values. The first 24 points in the abscissa correspond to the control point  $x$  coordinates whereas the last 24 correspond to the  $y$  ones. The E-SI approach with full differentiation of the turbulence model coincides with FD. It is interesting to note that the  $SI$ -based SD need to be divided by 50 in order to match the scale of the correct SD. From Ref. 10.

where  $\tilde{v}_a$  is the adjoint to the turbulence model variable  $\tilde{v}$  and  $R_{\tilde{v}}$  is the residual of the Spalart-Allmaras equation. In the  $k-\epsilon$  or the  $k-\omega$  SST models, this new integral must be replaced by  $\int_{\Omega_F} k_a R_k d\Omega + \int_{\Omega_F} \epsilon_a R_\epsilon d\Omega$  or  $\int_{\Omega_F} k_a R_k d\Omega + \int_{\Omega_F} \omega_a R_\omega d\Omega$  respectively, where the computation of the new adjoint fields requires the formulation and solution of extra PDEs. After zeroing the multipliers of  $\delta p/\delta b_n$ ,  $\delta v_i/\delta b_n$ ,  $\delta T^D/\delta b_n$ ,  $D = F, S$  and  $\delta \tilde{v}/\delta b_n$  (for the Spalart-Allmaras model), the adjoint PDEs arise. In the absence of field integrals in  $J^F$  and surface integrals in  $J^S$ , the system of the adjoint PDEs, for the Spalart-Allmaras model, becomes

$$R_q = -\frac{\partial u_j}{\partial x_j} = 0 \quad (16a)$$

$$R_{u_i} = u_j \frac{\partial v_j}{\partial x_i} - \frac{\partial (v_j u_i)}{\partial x_j} - \frac{\partial \tau_{ij}^a}{\partial x_j} + \frac{\partial q}{\partial x_i} + \mathcal{E} \rho_F \left[ c_p T_a^F \frac{\partial T^F}{\partial x_i} + T_a^F v_k \frac{\partial v_k}{\partial x_i} - v_i v_k \frac{\partial T_a^F}{\partial x_k} \right] + u_k \frac{\partial f_k}{\partial v_i} + AMS_i = 0, \quad i = 1, 2, (3) \quad (16b)$$

$$R_{T_a^F} = -v_j \frac{\partial T_a^F}{\partial x_j} - \frac{\partial}{\partial x_j} \left( \alpha_{eff} \frac{\partial T_a^F}{\partial x_j} \right) = 0 \quad (16c)$$

$$R_{T_a^S} = -\frac{\partial}{\partial x_j} \left( k^S \frac{\partial T_a^S}{\partial x_j} \right) + J_\Omega^S = 0 \quad (16d)$$

$$R_{\tilde{v}_a} = -\frac{\partial (v_j \tilde{v}_a)}{\partial x_j} - \frac{\partial}{\partial x_j} \left[ \left( \frac{\nu + \tilde{v}}{\sigma} \right) \frac{\partial \tilde{v}_a}{\partial x_j} \right] + \frac{1}{\sigma} \frac{\partial \tilde{v}_a}{\partial x_j} \frac{\partial \tilde{v}}{\partial x_j} + 2 \frac{c_{b2}}{\sigma} \frac{\partial}{\partial x_j} \left( \tilde{v}_a \frac{\partial \tilde{v}}{\partial x_j} \right) + \tilde{v}_a \tilde{\mathcal{C}}_{\tilde{v}} + \frac{\partial v_t}{\partial \tilde{v}} \frac{\partial u_i}{\partial x_j} \left( \frac{\partial v_i}{\partial x_j} + \frac{\partial v_j}{\partial x_i} \right) + (-P(\tilde{v}) + D(\tilde{v})) \tilde{v}_a + \tilde{v}_a \frac{\partial f^{\tilde{v}}}{\partial \tilde{v}} + \mathcal{E} \rho_F \frac{c_p}{Pr_t} \frac{\partial T_a^F}{\partial x_j} \frac{\partial T^F}{\partial x_j} \frac{\partial v_t}{\partial \tilde{v}} = 0 \quad (16e)$$

where  $P(\tilde{v})$  and  $D(\tilde{v})$  are the production and dissipation terms of the model and  $f^{\tilde{v}}$  is an extra term emerging from possible source terms in  $R_{\tilde{v}}$  including  $\tilde{v}$  (as in the case of topology optimization, see section II.C). Among other variables,  $D(\tilde{v})$  depends on the distance  $\Delta$  from the wall. The extra terms contained in the  $AMS_i$  term in eq. 16b arise from the differentiation of the turbulence model<sup>23,24</sup> and would not exist if the “frozen turbulence” assumption was made; the same holds for the last term in Eq. 16e. The adjoint boundary conditions are derived by properly treating the boundary integrals that depend on variations in the flow variables. In the E-SI adjoint formulation, the adjoint grid displacement equations should additionally be solved as explained in section II.A.3.

Additional terms also arise in the SD expressions. For instance, following the  $SI$  formulation, the term  $TMT = \int_{S_{F,W}} \left[ -(\nu + \frac{\tilde{v}}{\sigma}) \frac{\partial \tilde{v}_a}{\partial x_j} n_j + \frac{\partial J_{S_m}}{\partial \tilde{v}} n_m \right] \frac{\partial \tilde{v}}{\partial x_k} \frac{\delta x_k}{\delta b_n} dS$  should be added to the RHS of Eq. 8, and additional

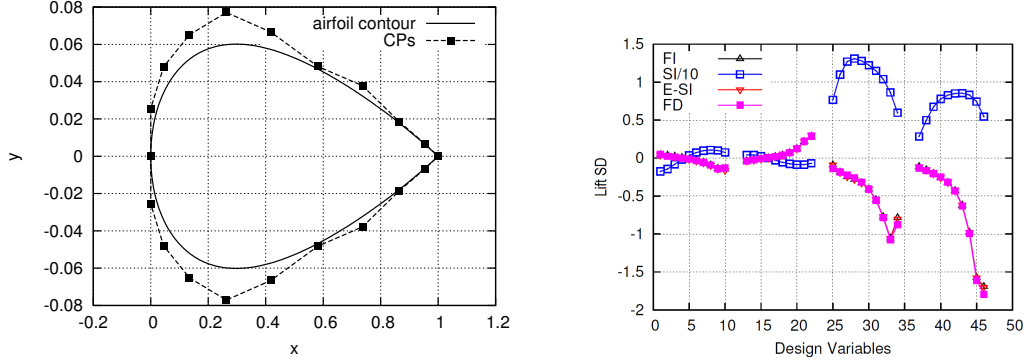


Figure 2. Turbulent flow around the NACA0012 airfoil ( $Re=10^6$ ,  $a_\infty=3^\circ$ , average  $y^+=0.2$  along the wall). (a) Airfoil geometry (not in scale) parameterized with 24 control points. (b) Comparison of the lift SD computed by the *FI*, *SI*, *E-SI* and *FD* methods. SD are computed w.r.t. the  $x$  (first half points in the abscissa) and  $y$  (second half) coordinates of 24 control points parameterizing the pressure and suction sides. The *SI* results have been divided by 10 in order to be on the same scale with those of the other methods. All adjoint variables presented include the differentiation of the turbulence model, see section II.B. Similarly to the previous case, figure 1, the *SI*-based SD differ considerably from *FD* and have the wrong sign for almost all design variables. In contrast, the *E-SI* approach computes the reference SD values. From Ref. 10.

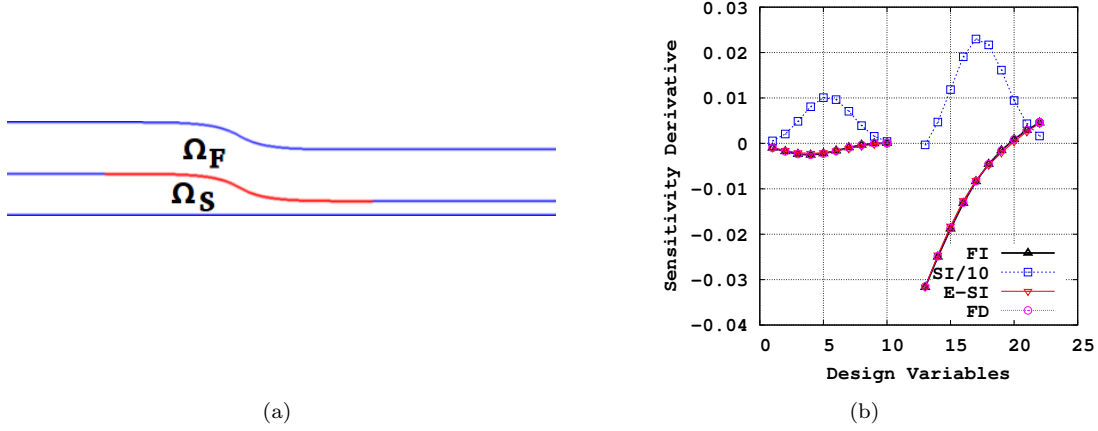


Figure 3. A CHT example: Laminar flow in an S-Bend 2D duct ( $Re=40$ ), attached to a solid body. Minimization of the mean temperature over the solid domain  $\Omega_S$ . (a) The fluid ( $\Omega_F$ ) and solid ( $\Omega_S$ ) domains along with the parameterized patch (red line). A NURBS curve with 12 control points is used to parameterize this part of the FSI, the  $x$  and  $y$  coordinates of which act as the design variables. (b) Comparison of SD computed with the *FI*, *E-SI*, *SI* adjoint and *FD*. It can be observed that even in this very simple example, the *SI* approach computes the wrong SD, which are an order of magnitude off and have the wrong sign for almost all design variables.

terms similarly need to be added to Eq. 15a if the *E-SI* approach is used. To account for the differentiation of the distance  $\Delta$  from the wall, i.e. to take into consideration  $\delta\Delta/\delta b_n$ , the Hamilton-Jacobi equation ( $R_\Delta = \frac{\partial(c_j\Delta)}{\partial x_j} - \Delta \frac{\partial^2\Delta}{\partial x_j^2} - 1 = 0$ , where  $c_j = \partial\Delta/\partial x_j$ ) is used as the PDE governing  $\Delta$ .<sup>5,27</sup> Then,  $L$  is extended by adding  $\int_{\Omega_F} \Delta_a R_\Delta d\Omega$  in Eq. 1 and a new adjoint PDE, in the form of  $R_{\Delta_a} = -2\frac{\partial}{\partial x_j} \left( \Delta_a \frac{\partial\Delta}{\partial x_j} \right) + \tilde{\nu}\tilde{\nu}_a C_\Delta = 0$ , for the adjoint distance  $\Delta_a$ , is derived and solved. In such a case, term TMT is further expanded by the integral  $\int_{S_{F,W}} \left( -2\Delta_a \frac{\partial\Delta}{\partial x_j} n_j \frac{\partial\Delta}{\partial x_k} + \Delta_a R_\Delta n_k \right) \frac{\delta x_k}{\delta b_n} dS$ . A convincing example demonstrating the need of solving the adjoint turbulence model equations can be found in figure 4.

A second example is presented in figure 5. It is about a similar CHT problem to the one presented in figure 3; however, here, the flow in the S-bend duct is turbulent ( $Re = 10^4$ ). The objective here is to minimize the part of the solid domain which has a temperature above a critical threshold,  $T_{crit}$ . To allow the mathematical formulation of the adjoint problem with such a non-differentiable objective, the latter is

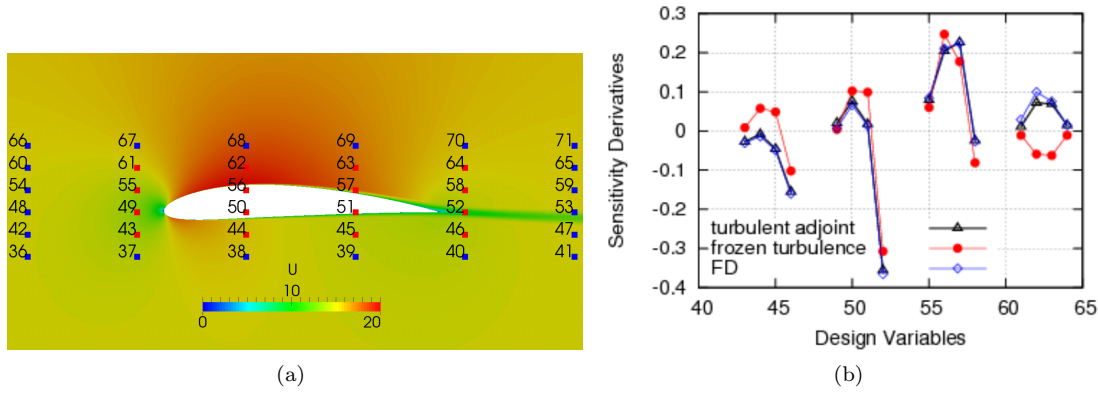


Figure 4. Drag sensitivities for the NACA4412 isolated airfoil; the flow is turbulent ( $Re = 1.5 \times 10^6$ ,  $a_\infty = 0^\circ$ ). A grid with 60000 cells is used, with an average  $y^+$  value of the first cell centers off the wall of 0.03. Adjoint to the low-Re Spalart–Allmaras model: Left: velocity magnitude field. A volumetric B-Splines morpher is used to parameterize the airfoil. The control grid of the morpher is plotted on top of the airfoil, along with the ID of each control point. Blue control points are kept fixed and only the red ones are allowed to move. Right: drag SD w.r.t. the  $y$  displacements of the control points. Three SD distributions are compared, corresponding to the “turbulent adjoint”, the adjoint approach making the “frozen turbulence” assumption and FD. The abscissa stands for the control point IDs. Note that by making the “frozen turbulence” assumption, wrongly signed SD are computed for control points 43 to 45 and 61 to 64. From Ref. 28.

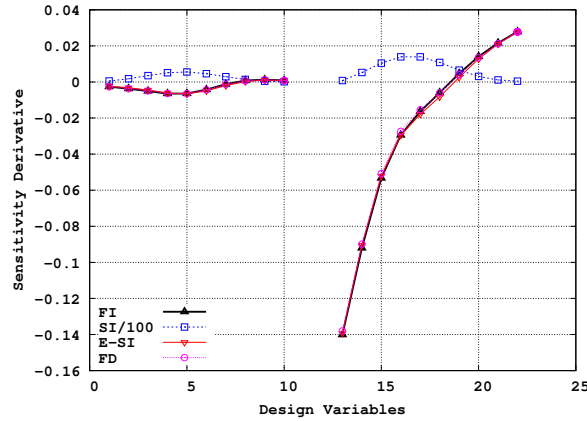


Figure 5. CHT problem: Turbulent flow in an S-Bend 2D duct ( $Re = 10^4$ ,  $Pr = 0.1$ ), attached to a solid body. Minimization of  $J_{maxT}$ , Eq. 17, over the solid domain  $\Omega_S$ . Comparison of SD computed with FI, E-SI, SI and FD methods. It can be observed that the SI approach computes the wrong SD, which are two orders of magnitude off and have an erroneous sign for almost all design variables.

approximated by the following sigmoid function defined in the interior of  $\Omega_S$

$$J^S = J_{maxT} = \frac{\int_{\Omega_S} \left[ 1 - \frac{1}{1 + e^{k_2(T^S - T_{crit}) + k_1}} \right] d\Omega}{\int_{\Omega_S} d\Omega} \quad (17)$$

where  $k_1 = \log\left(\frac{1}{1 - f_{max}} - 1\right)$ ,  $k_2 = \frac{\log\left(\frac{1}{1 - f_{min}} - 1\right) - k_1}{T_{safe} - T_{crit}}$ .

### C. Topology Optimization

Topology optimization introduces a vectorial source term into the RHS of the momentum equations (in the form of the external force term  $f_i(\vec{v}, \vec{b})$  in Eq. 4) which contains a scalar design variable for each grid cell and is controlled to minimize an objective function; the form of the additional source term varies depending on the topological approach utilized.<sup>14,15</sup> The topological approach of this paper employs the level set method<sup>29</sup> and therefore defines the design variable in each grid cell as the value of the level set signed-distance field ( $\phi$ )

which maps the moving interface  $\Gamma$  between the solid and fluid topological domains. Thus,  $J^F$  is minimized by computing the optimal location of  $\Gamma$ . The source term has a continuously differentiable, piecewise sigmoidal Heaviside relationship  $H$  to  $\phi$  and is scaled by a user-defined constant  $C_{MAX}$ , i.e.  $f_i(\vec{v}, \vec{b}) = C_{MAX}H(\phi)v_i$  in Eq. 4. For a cell  $m$ , if  $H(\phi_m)$  approaches 1, the source term becomes dominant, forcing the velocity toward zero and effectively obstructing flow in that cell. Conversely, if  $H(\phi_m)$  approaches 0, the flow is uninhibited. The differentiation of the force term leads to the following expression for the last term on the RHS of Eq. 7b,

$$u_k \frac{\partial f_k(\vec{v}, \vec{b})}{\partial v_i} = C_{MAX}H(\phi)u_i \quad (18)$$

The SD w.r.t. each computational cell  $m$ 's design variable  $\phi_m$  are given by Eq. 8, for which  $W_{1,m} = W_{2,m} = W_{3,m} = 0$  since the mesh node positions are kept fixed and  $W_{4,m}$  is defined as

$$W_{4,m} = \int_{\Omega} C_{MAX} \frac{\partial H(\phi)}{\partial \phi_m} v_i u_i d\Omega = C_{MAX} D(\phi_m) v_i^m u_i^m \Omega^m \quad (19)$$

where the scaled Heaviside function  $H(\phi)$  and its derivative  $D(\phi)$  depend only on the  $m$ -th grid cell with volume  $\Omega^m$  associated with the discrete description of the domain. To move  $\Gamma$  toward the optimal solution, the level set field is subjected to a process of convection by solving what is practically a steepest-descent step for the  $\phi$  field and applying eq. (19) as the convection velocity. Elaboration on the level set process as a whole is found in Ref. 19.

### III. Transition from Topology to Shape Optimization

This section deals with the synergistic use of 3D topology and shape optimization. Topology optimization is commonly employed in fluid mechanics to develop optimal internal-flow paths between topologically-ambiguous inlets and outlets, but itself produces solutions which are not CAD-compatible. In contrast, shape optimization may only alter boundaries of known connectivity within a geometry to search for an optimal solution, but uses far fewer design variables than topology and is inherently CAD-compatible if the parameters of the CAD model are used as the design variables. In addition, and unlike topology optimization, shape imposes proper boundary conditions, thus leading to a more physically accurate solution, especially if turbulent effects are being considered. By using the two methods in a synergistic manner, the drawbacks of both can be avoided: topology optimization can be employed to define a topologically correct set of inlet-outlet connections, and then shape optimization can be used to find a CAD-compatible solution which respects the proper boundary conditions. To achieve this synergistic optimization, a transition process for 3D geometries (developed in 2D in Ref. 19 and referred to as the TtoST -Topology to Shape Transition-process) is employed. The TtoST process is exemplified through a test case in section IV.A.

In this work, the implemented process of shape optimization takes parameterized NURBS surfaces as inputs in order to build an initial computational grid with a parameterized boundary. Thus, the goal of the TtoST process is to automatically generate and fit, as closely and efficiently as possible, NURBS to the optimal  $\Gamma$  found by topology. As discussed in section II.C, the topology process employed in this paper is level set based, meaning that  $\Gamma$  is the 0-level set of the optimal signed-distance field  $\phi$ . However, it should be noted that the solution to any topology optimization method could just as easily define  $\Gamma$ .

In preparation for the following explanation of the TtoST process, some terminology should first be defined. For the remainder of this paper, data associated with  $\Gamma$  will be referred to in the context of an 'iso-surface' and will thus be prefixed with 'iso' and capitalized. The isoSurface has three main domains: source, design and fixed. The source domain pertains to any inlet or outlet boundaries in a case's geometry. It is considered important to capture these aspects of a case to high precision as they help define the design space. Thus, they act as the origin from which much of the TtoST process' data are built. Points on the isoSurface in the source domain are found by boundary face-centers of the topology optimization case. The design domain pertains specifically to  $\Gamma$  or fluidized design walls. Thus, points of the isoSurface pertaining to the design domain are found through interpolation of  $\Gamma$ . Finally, the fixed domain pertains to any portions of the case which are walls excluded from the design space, such as entry channels. IsoSurface points of the fixed domain are also found via boundary face-centers of the topology optimization case. The TtoST process can be broken into two main steps:  $\Gamma$  sub-division and NURBS Initialization.

## A. IsoSurface ( $\Gamma$ ) Sub-Division

As the second half of the TtoST process (see section III.B) seeks to initialize NURBS surfaces via least-squares to represent the isoSurface, the first half seeks to provide the target information each NURBS surface requires for such an initialization. The sub-division algorithm thus partitions the isoSurface into discrete and contiguous areas dubbed ‘isoPatches’ which consist of both internal points and sets of bounding points called ‘facets’. Due to the mathematics of NURBS surfaces, we choose to require each isoPatch obeys the following criteria: (a) its internal and bounding isoSurface points are ordered; (b) each of its facets is shared with exactly one other isoPatch; (c) it has exactly four facets (as each NURBS surface has four sides); (d) it cannot represent more than one type of isoSurface domain.

The first major step in the sub-division process is to order the points of the isoSurface: doing this both allows for algorithmic simplicity and addresses isoPatch criterion (a). Through the known connectivity of the original case mesh, an unstructured surface-mesh referred to as the ‘isoMesh’ is built from the raw isoSurface data. The isoMesh initiates from the set of bounding contours of the source domains, meaning that the shape of all inlets and outlets is captured exactly. Point, face, and edge construction of the isoMesh then propagates out from the source domain limits until all isoSurface information is accounted for. During this construction, knowledge of what portions of the isoMesh pertain to which isoSurface domains is retained.

Each domain of the isoSurface can be considered as a 2-manifold  $\Sigma$ , i.e. a real  $\mathbb{R}^2$  coordinate space embedded in  $\mathbb{R}^3$  (for more on manifold theory, see Ref. 30). 2-manifolds have two main traits: a genus  $g$  which denotes how many holes exist in the manifold and a number of boundaries  $k$ . Thus, 2-manifolds are denoted  $\Sigma_{g,k}$ , and various examples of such manifolds can be seen in figure 6. As the goal of the sub-division process is to represent the isoSurface with a set of isoPatch manifolds  $\Sigma_{0,1}$ , it is integral that the topological traits of each of these inter-connected 2-manifolds be assessed.

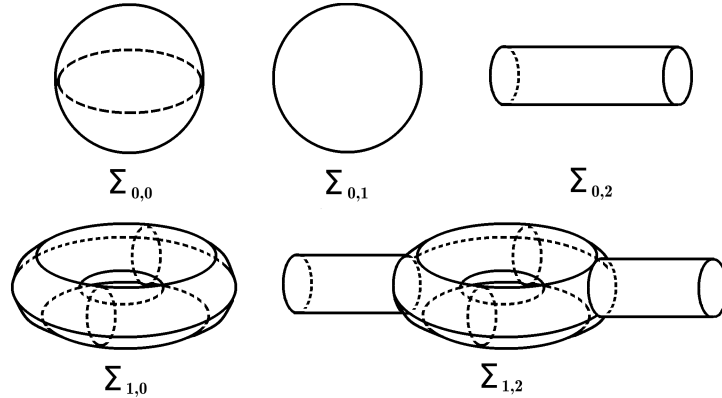


Figure 6. Examples of 2-manifolds with genus  $g$  and number of boundaries  $k$  denoted as  $\Sigma_{g,k}$ .

The number of boundaries of each isoSurface domain 2-manifold is known a-priori based on how the isoMesh was constructed. However, the genus of these manifolds is not known in this way and must be mapped to find holes, bifurcations, and junctions (if any). This is done by first building a Morse function<sup>31</sup> on the manifold’s surface. A Morse function is a real-valued function defined on a compact smooth manifold, and is chosen based on application.<sup>32</sup> For the work presented in this paper, the Laplace equation was selected as the Morse function. The Morse function is used to construct a Reeb graph,<sup>33</sup> which is a map of the topological change in the Morse function’s iso-contours. The Reeb graph construction process used is similar to that of Ref. 34, except it applies to surface meshes with varying types of elements, not just triangulated ones.

Using the information provided by the Reeb graph, each domain’s 2-manifold is broken into sub-manifolds such that all sub-manifolds have no holes ( $g = 0$ ). One sub-manifold boundary ( $k = 0$ ) is chosen as a base and the sub-manifold is cut between  $k = 0$  and all other  $k$ . making each sub-manifold of  $\Sigma_{0,1}$  topology. The edge of each sub-manifold is then broken into an even number of facets such that the facets of all touching sub-manifolds coincide, thereby making the sub-manifold an isoPatch. An example of this process can be seen for a 2-manifold in figure 7. These even-faceted sub-manifold isoPatches are subsequently internally

divided until all they have four sides, i.e. facets, and thus become ‘final’ isoPatches. Thus, all final isoPatches have criteria (b), (c), and (d) satisfied and the first major step in the TtoST process is complete.

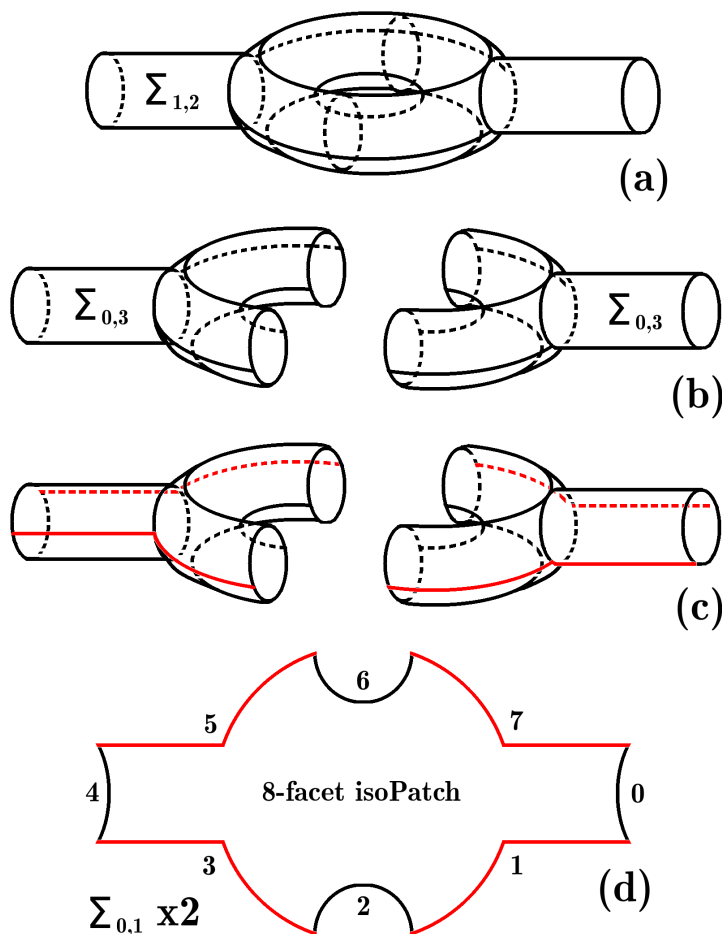


Figure 7. An example of sub-division of a  $\Sigma_{1,2}$  2-manifold. (a) The initial manifold: knowledge and location of the topological hole comes from Reeb-graph analysis (not shown). (b) The breaking of the original manifold into  $\Sigma_{0,X}$  (here,  $X$  turns out to be 3) sub-manifolds via division across the topological hole. (c) Cutting of the  $\Sigma_{0,X}$  sub-manifolds so that they become  $\Sigma_{0,1}$  2-manifolds. (d) The resulting isoPatches (both are identical) with 8 facets.

## B. IsoSurface NURBS Surface Initialization

The second major step is to initialize the set of NURBS surfaces which will represent the set of found isoPatches, and thus the entire isoSurface. NURBS surfaces have two parametric values,  $r_u$  and  $r_v$ , which range from 0 to 1, with a basis function associated with each. Thus a surface has four sides, each of which has one parameter fixed while the other increases between 0 and 1. Additionally, each basis function of a NURBS surface has a degree and a number of control points associated with it. Since we desire our NURBS surface set to be contiguous, each side of the NURBS surface should exactly match some other side of another surface, leading to the following requirements: the degree and number of control points of the basis functions should be the same for all surfaces, and the parametric velocity of the increasing parameter along each NURBS side should match that of the neighboring surface. We meet these requirements by building a set of NURBS curves, each of which represents a shared NURBS surface edge, and using those curves to supply the  $r_u$  or  $r_v$  data, as well as the degree and number of control points for that side of the sharing surfaces. Each curve has the same degree and number of control points. The curves are initialized via least-squares, with their target data being the points of a facet. Thus, a set of isoPatch facets-linkings termed ‘isoSeams’ is chosen as a target net for initializing these NURBS curves such that each pair of linked isoPatch facets is

represented once.

All NURBS surfaces are initialized simultaneously by solving a constrained least squares system to find the control point positions which minimize the squared error of the surfaces' positions w.r.t. the system's target information. To do this, the points of the isoMesh belonging to each isoPatch must be given  $r_u$  and  $r_v$  parametric values. This is done by solving a Laplace equation on the isoPatch in both  $r_u$  and  $r_v$ . The goal of an unconstrained least-squares problem would be to get the NURBS surfaces to represent these parameterized points as closely as possible. However, solving this simple system would result in surfaces which would not be contiguous. Thus, constraints of coinciding interface control points are added to the least squares system through the method of augmented Lagrange multipliers such that all surface edges remain in contact. Similarly, for those NURBS surfaces which represent the isoSurface's design domain, additional targets are added to the least squares system which desire to enforce G1 continuity between interfacing surfaces. Once all NURBS surfaces are initialized, they can be used to build a parameterized surface mesh and finite-volume computational mesh from which shape optimization can begin.

## IV. Applications

### A. Synergistic Optimization Example: Transition of a Straight Tube

This section uses a topologically-simple case to exemplify the TtoST process which allows synergistic topology-shape optimization. The presented case has one inlet and outlet and entry channels which allow boundary-layer formation between them and the design domain. The inlet velocity profile is uniform such that the Reynolds number is 500. The kinematic viscosity is that of air ( $1.5 \times 10^{-5} \frac{m^2}{s}$ ). The objective function to be minimized is the volume-averaged total pressure losses between the inlet  $S_{F_I}$  and outlet  $S_{F_O}$  and is given by

$$J^F = J_{p_t} = - \int_{S_{F_I}} \left( p + \frac{1}{2} v_k^2 \right) v_i n_i dS - \int_{S_{F_O}} \left( p + \frac{1}{2} v_k^2 \right) v_i n_i dS \quad (20)$$

where  $n_i$  are the components of the outward (from the fluid to boundary) normal vector.

The initial geometry and level set topology solution  $\Gamma$  can be seen in figure 8(a). The TtoST process begins by assessing this solution to form an isoSurface, finding source, fixed, and design domains which will be respected as separate during the sub-division of the isoSurface. The isoMesh, shown in figure 8(b), is built across the isoSurface from the bounding contours of the source domains and retains the domains of the isoSurface. Once the isoMesh has been built, 2-manifolds are constructed which represent each individual domain and a Reeb-graph analysis is performed on each manifold to check for topological holes or bifurcations. The Laplace Morse functions built on the 2-manifolds' surfaces, as well as the Reeb graphs themselves, are found in figure 8(c). As no holes or bifurcations exist in the tube or its entrance channels, subdivision proceeds, resulting in the isoSurface being divided into 14 isoPatches: one for each inlet and outlet, four for each entrance channel and four for the design domain. The points of each patch are given the parametric values  $r_u$  or  $r_v$  required to initialize their NURBS surfaces with least-squares. The parameterized isoPatches which make up the isoSurface can be seen in figures 8(d) and 8(e). Using the parameterized isoPatch set as a source, the set of NURBS surfaces which will represent the isoSurface and be used to initialize shape optimization is initialized using least squares. Each surface is initialized with 8 control points in both parametric directions and a degree of 5. The initialized surfaces, overlaid with the outlines of their target isoPatches, as well as their control point nets, can be found in figure 8(f).

Starting from the set of parameterized NURBS surfaces depicted in figure 8(f), a body fitted mesh of  $\sim 5 \times 10^5$  cells is constructed and used to conduct a shape optimization. The objective to be minimized is  $J_{p_t}^F$  with the constraint of continuous first-order derivatives along the interfaces, i.e.

$$C_{G1} = \sum_{i=1}^{n_e} \left( \left. \frac{\partial \vec{x}_i}{\partial w} \right|_{S_1} - \left. \frac{\partial \vec{x}_i}{\partial w} \right|_{S_2} \right)^2 \quad (21)$$

where  $n_e$  is the total number of interface points of the control surfaces,  $S_1$  and  $S_2$  are two adjacent NURBS surfaces and  $w$  the parametric coordinate w.r.t. which derivative continuity has to be imposed. It should be mentioned that G1 continuity along one of the parametric coordinates is ensured by construction, since the boundary curves of the adjacent surfaces share the same control points. The constraint is treated as

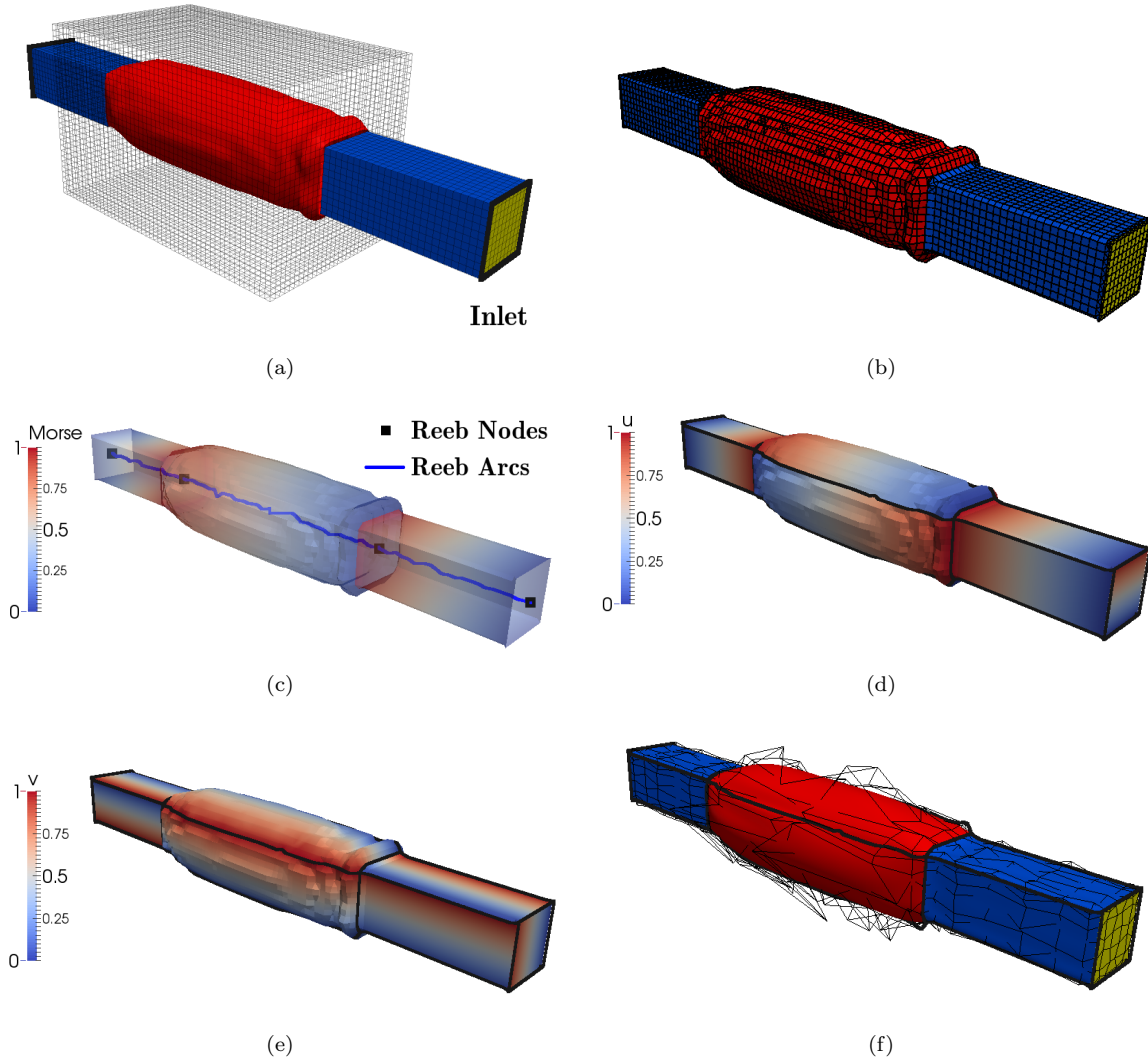


Figure 8. TtoST of a tube: (a) The topological solution (i.e. isoSurface) of the tube case. The inlet and outlet (not shown) of the topology case (i.e. the isoSurface's source domain) are denoted in yellow, the entry channels (i.e. the fixed domain) in blue, and  $\Gamma$  (i.e. the design domain) in red. The outer bounds of the source domain are denoted with solid black lines. (b) The unstructured isoMesh which is built outward from the source domain's outer bounds using the geometry of the topology case. Portions of the isoMesh corresponding to the source, fixed, and design domains are denoted as yellow, blue, and red, respectively. Each domain is represented by a 2-manifold. (c) The Reeb-analysis of the 2-manifolds. The Laplacian Morse function varies between 0 and 1 on each manifold and its iso-contours are tracked to build its Reeb graph: Black dots denote Reeb nodes and blue lines denote Reeb arcs. The Reeb graphs' structures are such that no topological variance exists. (d and e) The parametric values assigned to the points of each isoPatch representing the isoSurface. (f) The initialized degree 5 NURBS surfaces and their  $8 \times 8$  control point nets. Surfaces pertaining to the source, fixed, and design domains of the isoSurface are denoted in yellow, blue, and red, respectively.

an equality one ( $C_{G1} = 0$ ) and is imposed by using the SQP method.<sup>35</sup> Only the control points of the surfaces marked in red in figure 8(f) are allowed to vary, giving rise to an optimization problem with  $\sim 570$  design variables. The convergence of the objective and constraint functions are depicted in figure 9. A small reduction of  $\sim 0.5\%$  is observed for  $J_{pi}^F$ ; this can be attributed to the fact that the initial geometry coming from the TtoST process was already close to the optimal solution. On the contrary, the  $C_{G1}$  value has been considerably reduced by  $\sim 65\%$ . The interface points/areas contributing to  $C_{G1}$  in the initial and optimized geometries are shown in figure 10. A comparison between the initial and optimized geometries is given in figure 11.

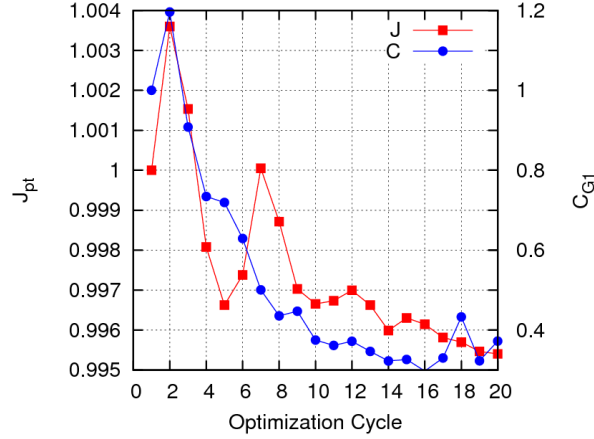


Figure 9. Shape optimization of the straight tube: Convergence of the objective and constraint values, plotted over the left and right axes, respectively. Both metrics are normalized on their respective initial values. Since no line search was used and the initial geometry coming from the TtoST process was already close to the optimal solution, the first optimization step overshoot the minimum. However, the algorithm recovered in the next steps, leading to a  $J_{pt}^F$  reduction of  $\sim 0.5\%$  and a  $C_{G1}$  reduction of  $\sim 65\%$ .

## B. Shape Optimization: Lift-to-Drag Ratio Maximization for a Glider Plane

This section is concerned with the improvement of the aerodynamic design of an industrial glider flying at high angles of attack. Its principal target is to reduce the separation occurring in the wing-fuselage junction region of the original design of the Taurus Electro glider at high incidence angles using an adjoint-based optimization algorithm. Such an optimization is performed by updating the local geometry of the fuselage and fairing, maintaining the wing airfoil unchanged. The Taurus Electro glider, designed and manufactured by Pipistrel d.o.o. Ajdovščina Slovenia, figure 12, is a two-seat electric self-launching ultra-light glider made out of composite materials. The wing is located in a vertically central position w.r.t. the fuselage whilst its longitudinal position is aft the maximum height section, behind the cockpit, in a positive pressure gradient area. This configuration implies that, in the fuselage junction region, the wing suffers an extra increase of flow velocity close to the leading edge and an increased adverse pressure gradient in the trailing edge region that cause a leading edge separation at high angles of attack (AoA). Although the separation is not critical and an ordinary pilot doesn't fly in conditions when this happens, it is still interesting to explore the occurrence. The target is to diminish the separation region and, consequently, enhance the aerodynamic efficiency of the whole glider at these conditions. The optimization problem targets the maximization of the lift-to-drag ratio or, equivalently, the minimization of

$$J^F = J_{L/D} = - \frac{\int_{S_W} (-\tau_{ij} n_j + p n_i) r_i^L dS}{\int_{S_W} (-\tau_{ij} n_j + p n_i) r_i^D dS} \quad (22)$$

where  $\mathbf{r}^L$  and  $\mathbf{r}^D$  are the lift and drag force projection (unit) directions, respectively. This case comes from the RBF4AERO Project which aimed at developing the RBF4AERO Benchmark Technology and was presented in Ref. 36. The flow Reynolds number is  $Re = 1.55 \times 10^6$  based on the wing chord, the Spalart–Allmaras turbulence model is used, the mesh consists of about 4.7 million cells and the far-field flow angle is  $10^\circ$ . The geometry is parameterized using four RBF-based design variables<sup>36,37</sup> depicted in figure 13, controlling the wing-fuselage junction close to the leading and trailing edges as well as parts of the upper fuselage surface. The convergence of the steepest descent-driven algorithm can be found in figure 14(a). It can be observed that the lift-to-drag ratio has increased by 15%, caused by 10% drag reduction and a 4% lift increase. The optimized geometry is illustrated in figure 14(b). In figure 15, the near-wall velocity isolines are plotted on the glider surface for the initial and optimized geometries. It can be observed that the flow recirculation formed close to the trailing edge-fuselage junction has been significantly reduced.

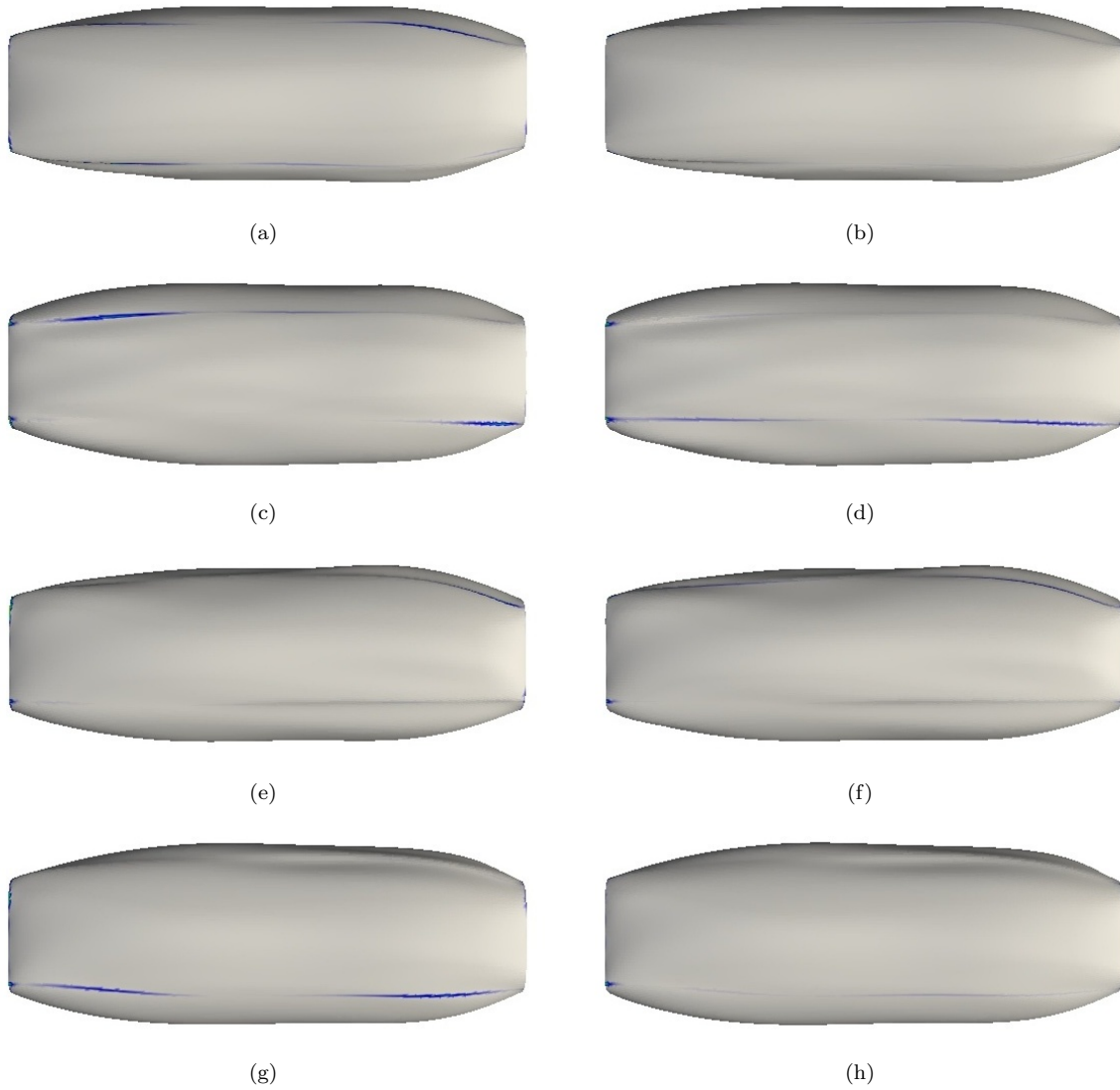


Figure 10. Shape optimization of the straight tube: Contribution of the interface points to the  $C_{G1}$  constraint value, for the initial (left column) and optimized (right column) geometries, as seen from various viewpoints (top-to-bottom). Gray areas correspond to zero contributions whereas purple ones to large contributions. In most areas, the optimized geometry has a smoother  $G1$  transition between surfaces than the initial one.

### C. Shape Optimization: Car Engine Cylinder Head Cooling

In this section, the shape optimization of a simplified, internally cooled cylinder head of a car engine is presented. The geometry (provided by Volkswagen AG), as seen in figure 16, consists of three groups of boundaries; a) the outer rectangular surface (with light gray color) which is an adiabatic boundary, b) the air-intake, the four cylinder-heads, and the four exhaust pipes (with dark grey color), which have constant heat flux boundary conditions, and c) the cooling channels (whose surfaces are the FSI boundaries, colored with purple) through which coolant flows in order to lower the temperature of the cylinder head. The flow of the coolant (Eqs. 4a to 4c) is solved in the region inside the pipe with purple color, whereas the heat conduction PDE (Eq. 4d) is solved for the region between the outer surface and the boundaries of the air-intake manifold, the cylinder heads and the exhaust pipes. The coolant flow is turbulent (the Spalart-Allmaras turbulence model is used) and the non-FSI wall boundaries of the fluid domain are assumed to be adiabatic.

The objective function to be minimized is defined over  $\Omega_S$  and is a modified version of Eq. 17, given by

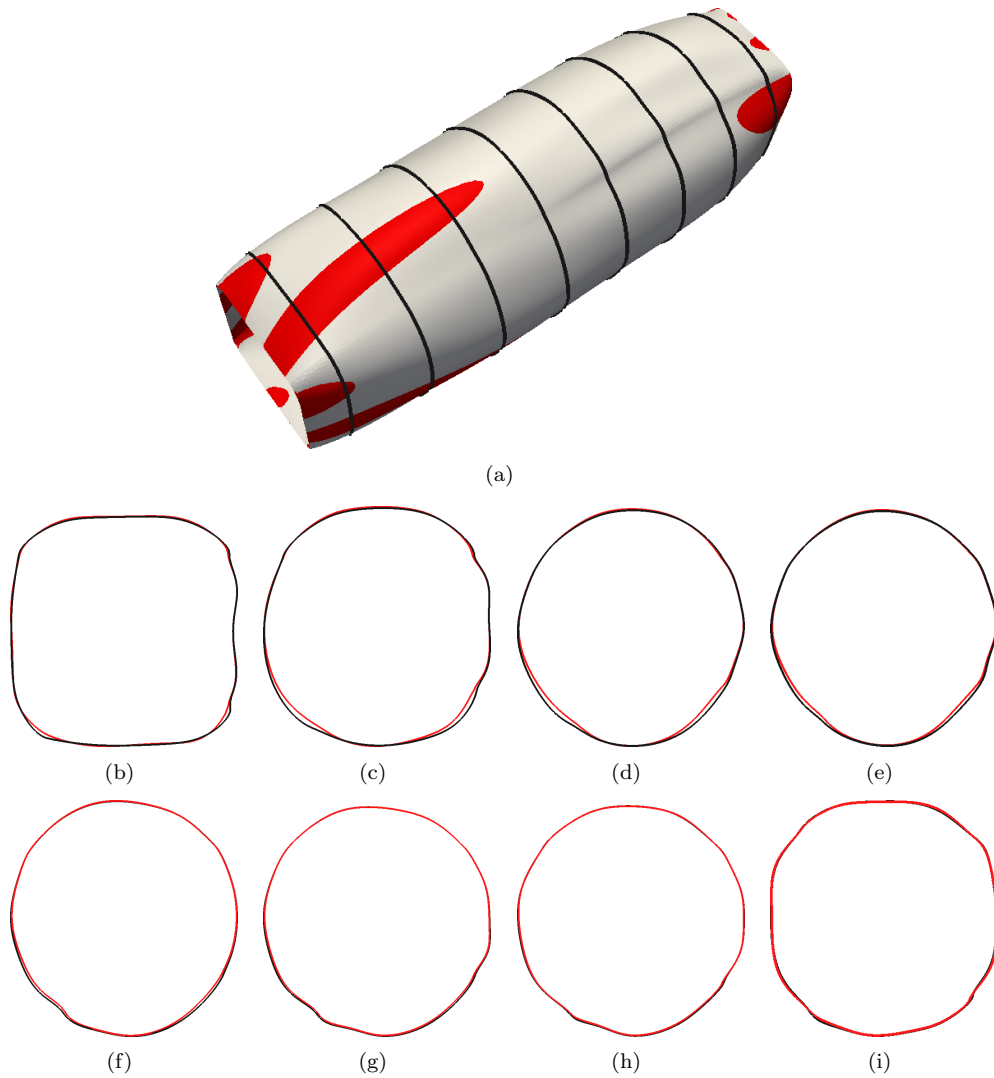


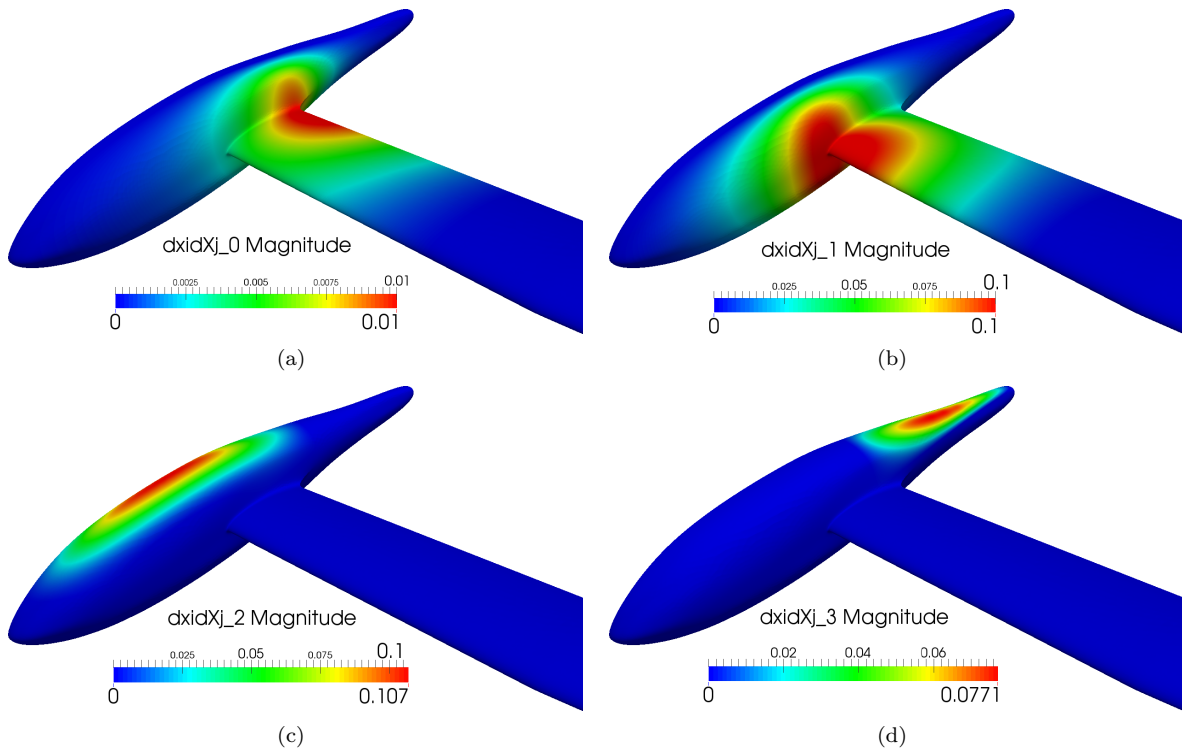
Figure 11. Shape optimization of the straight tube: (a) Overlay of the parameterized parts of the initial (gray) and optimized (red) geometries, along with the position of 8 slices. The slices are used to compare cross sections (b to i, ordered from left to right) of the initial (black) and optimized (red) geometries. Flow direction is from left to right. The main changes are observed in the first half of the duct.



Figure 12. The Taurus Electro glider.

the following continuously differentiable piecewise function

$$J^S = J_{penT} = \begin{cases} J_{maxT} & \text{if } T^S \leq T_{crit} \\ \frac{\int_{\Omega_S} [\alpha(T^S - T_{crit}) + \beta] d\Omega}{\int_{\Omega_S} d\Omega} & \text{if } T^S > T_{crit} \end{cases} \quad (23)$$



**Figure 13. Shape optimization of a glider: Minimization of the lift-to-drag ratio ( $L/D$ ).** The grid sensitivities  $\delta x_k/\delta b_n$  on the surface of the glider (i.e. parameterization) are presented.  $\delta x_k/\delta b_n$  at the fuselage-wing junction close to the leading and trailing edge are shown in (a) and (b) respectively. In (c) and (d),  $\delta x_k/\delta b_n$  on the front and rear part of the fuselage are presented. The variation of the design variables is limited so that, after the optimization, manufacturable solutions arise.

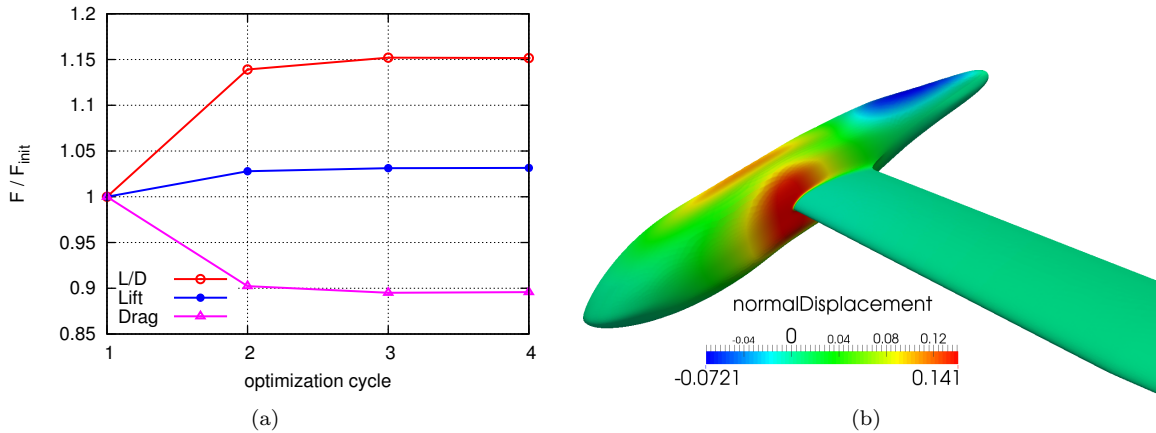


**Figure 14. Shape optimization of a glider: Minimization of the lift-to-drag ratio ( $L/D$ ).** In (a) the convergence of the objective function is presented. A 15% lift-to-drag increase is observed after 4 optimization cycles by mainly reducing the drag value and slightly increasing lift. In (b) the cumulative normal displacement of the glider surface is plotted over the optimized geometry. The areas mostly changed are those close to the wing-fuselage junction near the leading edge and at the top of the fuselage, where a maximum displacement of 14.1 cm arisen after the optimization.

where  $\alpha = \frac{k_2 e^{k_1}}{(1+e^{k_1})^2}$ ,  $\beta = \frac{e^{k_1}}{1+e^{k_1}}$  and  $k_1$  and  $k_2$  are constants as in Eq. 17.

The parameterization of the geometry can be seen in figure 17. After 8 optimization cycles, the objective function has dropped by 16.21%. In figure 18, the initial and optimized geometries are presented, whereas the temperature distribution along the FSI at the initial and optimized geometry are depicted in figure 19.

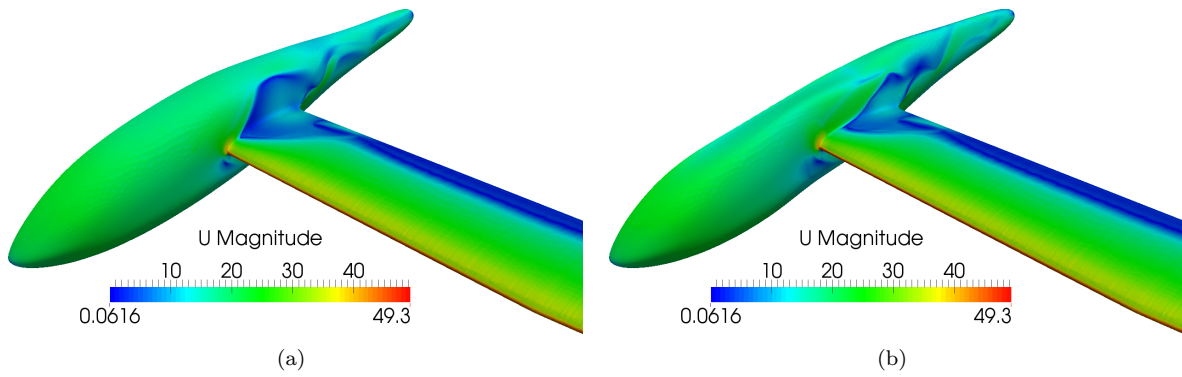


Figure 15. Shape optimization of a glider: Minimization of the lift-to-drag ratio ( $L/D$ ). The near wall velocity, plotted over the initial (a) and optimized (b) geometry are presented.

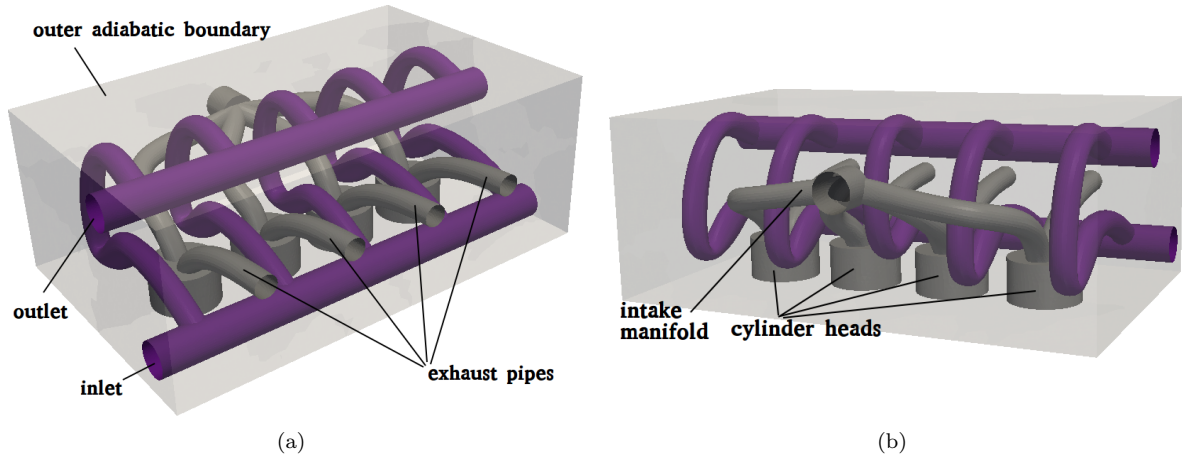


Figure 16. Cooled cylinder head of a car engine. Front (a) and rear (b) view of the geometry. The outer rectangular surface is an adiabatic boundary (light gray color), whereas constant heat flux is imposed along the air-intake manifold, the four cylinder heads and the exhaust pipe (dark gray). Along the FSI boundary, Eqs. 5 and 6 hold (purple). The coolant enters from the left of the lower horizontal pipe (a) and exits from the left of the upper horizontal pipe. The two other ends of the lower and upper horizontal pipes, are closed adiabatic boundaries.

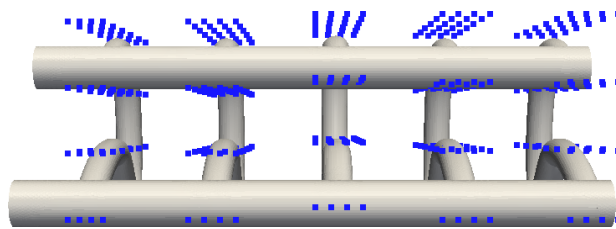


Figure 17. Cooled cylinder head of a car engine. Parameterization of the geometry using five sets of  $4 \times 4 \times 6$  control boxes that parameterize each of the five curved ducts connecting the two horizontal ducts.

Out of the five curved ducts connecting the horizontal ones, the optimization algorithm chose to mainly deform the three central ones. The area with the highest deformation in all curved ducts is that with the highest curvature. There, the cross-section area of the pipes became smaller, leading to a higher velocity magnitude and a locally increased head conduction.

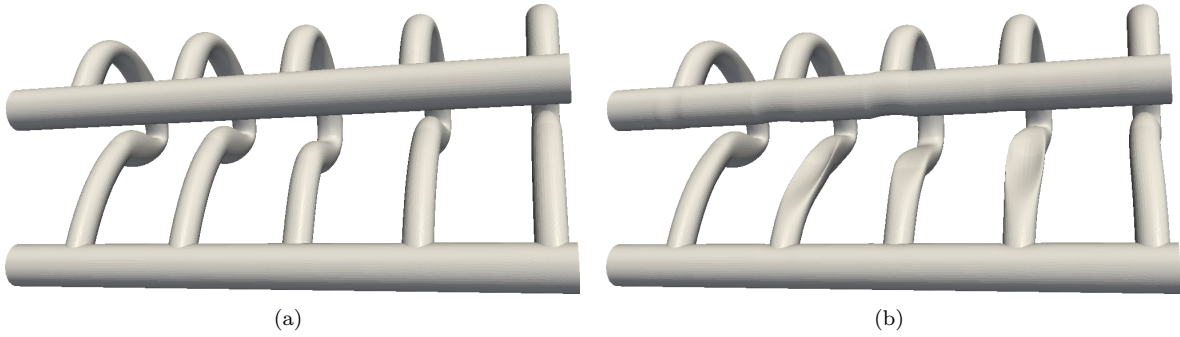


Figure 18. Cooled cylinder head of a car engine. Minimization of  $J_{penT}$ . Initial (a) and optimized (b) geometries. The areas mostly changed after the optimization are those with the highest curvature on the curved ducts connecting the two horizontal ones.

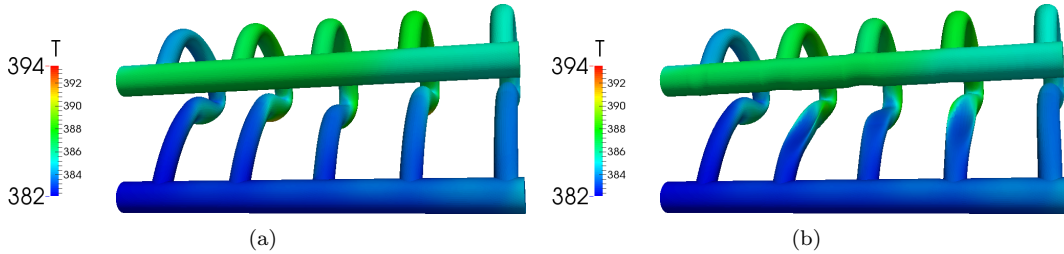


Figure 19. Cooled cylinder head of a car engine. Minimization of  $J_{penT}$ . Distribution of temperature along the FSI boundary at the initial (a) and optimized (b) geometries.

## V. Conclusion

A general framework for the continuous adjoint method was presented, in which the Enhanced Surface Integral (E-*SI*) formulation was shown to generate accurate sensitivity derivatives at low computational cost as it consists entirely of surface integrals and avoids the computation of grid sensitivities in the interior of the computational domain. Additionally, the turbulence model PDEs were differentiated in order to overcome the “frozen turbulence assumption,” leading to accurate sensitivity derivatives computation. In this general framework, a level set topology formulation was also defined. Though fundamentally different methods, 3D topology and shape optimization were considered in a novel, synergistic framework in which topology optimization solutions are processed in order to refine them. This transitional ‘TtoST’ approach allows any topological ambiguities in a case to be rectified, while still producing an accurate and CAD-compatible solution with proper boundary conditions. The 3D TtoST method was demonstrated to minimize the volume-averaged total pressure losses of a tube geometry, with shape improving the solution topology found. Shape optimization was performed to maximize the lift-to-drag ratio of a glider plane in which the E-*SI* method and the differentiated Spalart-Allmaras turbulence model were used produce accurate sensitivities. Finally, the E-*SI* method and differentiated Spalart-Allmaras turbulence model were applied to a shape optimization of a conjugate heat transfer problem in which the solid area of a cooled cylinder head with temperature above a critical value was minimized.

## Acknowledgments

The second author is an IODA Early Stage Researcher and was funded by the People Programme (ITN Marie Curie Actions) of the European Union’s H2020 Framework Programme (MSCA-ITN-2014-ETN) under REA Grant Agreement no. 642959 (IODA project). The PhD Thesis of the third author is funded by the General Secretariat for Research and Technology (GSRT) and the Hellenic Foundation for Research and Innovation (HFRI). The authors would like to thank Matej Andrejašič of Pipistrel d.o.o. Ajdovščina Slovenia and Hauke Narten of Volkswagen AG for providing the Taurus Electro glider and cylinder head cases and allowing their publication.

## References

- <sup>1</sup>Pironneau, O., *Optimal Shape Design for Elliptic Systems.*, Springer-Verlag, New York, 1984.
- <sup>2</sup>Jameson, A., “Aerodynamic Design via Control Theory.” *Journal of Scientific Computing*, Vol. 3, 1988, pp. 233–260.
- <sup>3</sup>Anderson, W. and Venkatakrishnan, V., “Aerodynamic Design Optimization on Unstructured Grids with a Continuous Adjoint Formulation.” *AIAA Paper*, Vol. 06, No. 43, 1997.
- <sup>4</sup>Papadimitriou, D. and Giannakoglou, K., “Aerodynamic Shape Optimization Using First and Second Order Adjoint and Direct Approaches,” *Archives of Computational Methods in Engineering*, Vol. 15, No. 4, 2008, pp. 447–488.
- <sup>5</sup>Papoutsis-Kiachagias, E. and Giannakoglou, K., “Continuous Adjoint Methods for Turbulent Flows, Applied to Shape and Topology Optimization: Industrial Applications.” *Archives of Computational Methods in Engineering*, Vol. 23, No. 2, 2016, pp. 255–299.
- <sup>6</sup>Jameson, A., Pierce, N., and Martinelli, L., “Optimum Aerodynamic Design Using the Navier-Stokes Equations.” *Theoretical and Computational Fluid Dynamics*, Vol. 10, 1998, pp. 213–237.
- <sup>7</sup>Papadimitriou, D. and Giannakoglou, K., “A Continuous Adjoint Method with Objective Function Derivatives Based on Boundary Integrals for Inviscid and Viscous Flows.” *Journal of Computers & Fluids*, Vol. 36, No. 2, 2007, pp. 325–341.
- <sup>8</sup>Othmer, C., “A Continuous Adjoint Formulation for the Computation of Topological and Surface Sensitivities of Ducted Flows.” *International Journal for Numerical Methods in Fluids*, Vol. 58, No. 8, 2008, pp. 861–877.
- <sup>9</sup>Lozano, C., “Discrete Surprises in the Computation of Sensitivities from Boundary Integrals in the Continuous Adjoint Approach to Inviscid Aerodynamic Shape Optimization,” *Computers & Fluids*, Vol. 56, 2012, pp. 118–127.
- <sup>10</sup>Kavvadias, I., Papoutsis-Kiachagias, E., and Giannakoglou, K., “On the Proper Treatment of Grid Sensitivities in Continuous Adjoint Methods for Shape Optimization,” *Journal of Computational Physics*, Vol. 301, 2015, pp. 1–18.
- <sup>11</sup>Bendsoe, M. and Kikuchi, N., “Generating Optimal Topologies in Structural Design Using a Homogenization Method,” *Journal of Computer Methods in Applied Mechanics and Engineering*, Vol. 71, 1988, pp. 197–224.
- <sup>12</sup>Aage, N., Poulsen, T., Gersborg-Hansen, A., and Sigmund, O., “Topology Optimization of Large Scale Stokes Flow Problems.” *Structural and Multidisciplinary Optimization*, Vol. 35, 2008, pp. 175–180.
- <sup>13</sup>Borvall, T. and Peterson, J., “Topology Optimization of Fluids in Stokes Flow,” *International Journal for Numerical Methods in Fluids*, Vol. 41, 2003, pp. 77–107.
- <sup>14</sup>Guest, J. and Prevost, J., “Topology Optimization of Creeping Fluid Flows Using a Darcy-Stokes Finite Element.” *International Journal for Numerical Methods in Engineering*, Vol. 66, 2006, pp. 461–484.
- <sup>15</sup>Gersborg-Hansen, A., Sigmund, O., and Haber, R., “Topology Optimization of Channel Flow Problems,” *Structural and Multidisciplinary Optimization*, Vol. 30, 2005, pp. 181–192.
- <sup>16</sup>Deng, Y., Zhang, P., Liu, Y., Wu, Y., and Liu, Z., “Optimization of Unsteady Incompressible Navier-Stokes Flows Using Variational Level Set Method,” *International Journal for Numerical Methods In Fluids*, Vol. 71, No. 12, 2013, pp. 1475–1493.
- <sup>17</sup>Deaton, J. and Grandhi, R., “A Survey of Structural and Multidisciplinary Continuum Topology Optimization: Post 2000.” *Structural and Multidisciplinary Optimization.*, Vol. 49, No. 1, 2013, pp. 1–38.
- <sup>18</sup>Sigmund, O. and Maute, K., “Topology Optimization Approaches. A Comparative Review.” *Structural and Multidisciplinary Optimization.*, Vol. 48, No. 6, 2013, pp. 1031–1055.
- <sup>19</sup>Koch, J., Papoutsis-Kiachagias, E., and Giannakoglou, K., “Transition from Adjoint Level Set Topology to Shape Optimization for 2D Fluid Mechanics,” *Computers & Fluids*, Vol. 150, 2017, pp. 123–138.
- <sup>20</sup>Jameson, A. and Alonso, J., “Aerodynamic Shape Optimization Techniques Based on Control Theory.” *AIAA Paper*.
- <sup>21</sup>Jameson, A. and Kim, S., “Reduction of the Adjoint Gradient Formula in the Continuous Limit.” *AIAA paper 2003-0040, 41th Aerospace Sciences Meeting and Exhibit*, Reno, Nevada, January 2003.
- <sup>22</sup>Gkaragkounis, K., Papoutsis-Kiachagias, E., and Giannakoglou, K., “Conjugate Heat Transfer Shape Optimization Based on the Continuous Adjoint Method,” *VII International Conference on Computational Methods for Coupled Problems in Science and Engineering COUPLED PROBLEMS*, Rhodes Island, Greece, 12-14 June 2017.
- <sup>23</sup>Papoutsis-Kiachagias, E. and Giannakoglou, K., “Continuous Adjoint Methods for Turbulent Flows, Applied to Shape and Topology Optimization: Industrial Applications,” *Archives of Computational Methods in Engineering*, Vol. 23, No. 2, 2016, pp. 255–299.
- <sup>24</sup>Zymaris, A., Papadimitriou, D., Giannakoglou, K., and Othmer, C., “Continuous Adjoint Approach to the Spalart-Allmaras Turbulence Model for Incompressible Flows.” *Computers & Fluids*, Vol. 38, No. 8, 2009, pp. 1528–1538.
- <sup>25</sup>Papoutsis-Kiachagias, E., Zymaris, A., Kavvadias, I., Papadimitriou, D., and Giannakoglou, K., “The Continuous Adjoint Approach to the  $k-\epsilon$  Turbulence Model for Shape Optimization and Optimal Active Control of Turbulent Flows,” *Engineering Optimization*, Vol. 47, No. 3, 2015, pp. 370–389.
- <sup>26</sup>Kavvadias, I., Papoutsis-Kiachagias, E., Dimitrakopoulos, G., and Giannakoglou, K., “The Continuous Adjoint Approach to the  $k-\omega$  SST Turbulence Model with Applications in Shape Optimization,” *Engineering Optimization*, Vol. 47, No. 11, 2015, pp. 1523–1542.
- <sup>27</sup>Bueno-Orovio, A., Castro, C., Palacios, F., and ZuaZua, E., “Continuous Adjoint Approach for the SpalartAllmaras Model in Aerodynamic Optimization.” *AIAA Journal*, Vol. 50, No. 3, 2012, pp. 631–646.
- <sup>28</sup>Giannakoglou K. and Papoutsis-Kiachagias, E. and Kavvadias, I. and Gkaragkounis K., “Continuous Adjoint in Shape & Topology Optimization - Recent Developments & Applications,” *Seminar on Adjoint CFD Methods in Industry and Research*, Wiesbaden, Germany, 24 - 25 November 2016, pp. 43–52.
- <sup>29</sup>Osher, S. and Sethian, J., “Fronts Propagating with Curvature Dependent Speed: Algorithms Based on Hamilton-Jacobi Formulations.” *Journal of Computational Physics*, Vol. 79, No. 1, 1988, pp. 12–49.
- <sup>30</sup>Ahlfors, L. and Sario, L., *Riemann surfaces*, Princeton University Press, 1960.
- <sup>31</sup>Milnor, J., *Morse Theory*, Princeton University Press, 1963.
- <sup>32</sup>Biasotti, S., Giorgi, D., and andB. Falcidieno, M. S., “Reeb Graphs for Shape and Applications,” *Theoretical Computer Science*, Vol. 392, 2008, pp. 5–22.

<sup>33</sup>Reeb, G., “Sur Les Points Singuliers d’une Forme de Pfaff Compltement Integrale ou d’une Fonction Numrique,” *Comptes Rendus Acad. Sciences*, Vol. 222, 1946, pp. 847–849.

<sup>34</sup>Brandolini, L. and Piastra, M., “Computing the Reeb Graph for Triangle Meshes with Active Contours.” *Proceedings of the 1st International Conference on Pattern Recognition Applications and Methods*, Vilamoura, Algarve, Portugal, 6-8 February 2012, pp. 80–89.

<sup>35</sup>Nash, S. and Nocedal, J., “A Numerical Study of the Limited Memory BFGS Method and the truncated-Newton Method for Large Scale Optimization,” *SIAM Journal on Optimization*, Vol. 1, No. 3, 1991, pp. 358–372.

<sup>36</sup>Papoutsis-Kiachagias, E., Andrejašič, M., Porziani, S., Groth, C., Eržen, D., and Biancolini, M.E., e. a., “Combining an RBF-Based Morpher with Continuous Adjoint for Low-Speed Aeronautical Optimization Applications,” *ECCOMAS Congress 2016, VII European Congress on Computational Methods in Applied Sciences and Engineering*, Crete island, Greece, June 5-10 2016.

<sup>37</sup>Jakobsson, S. and Amoignon, O., “Mesh Deformation Using Radial Basis Functions for Gradient-Based Aerodynamic Shape Optimization.” *Computers & Fluids*, Vol. 36, 2007, pp. 1119–1136.